Taylor & Francis
Taylor & Francis Group

REPORT

🔓 OPEN ACCESS | Check for updates

Structure-based engineering of a novel CD3ε-targeting antibody for reduced polyreactivity

Catherine Y Liu[a], Cory L Ahonen[a], Michael E Brown[a], Ling Zhou[a], Martin Welin[b], Eric M Krauland[a], Robert Pejchal[a], Paul F Widboom[a], and Michael B Battles [iD][a]

[a]Adimab, LLC, NH, USA; [b]SARomics Biostructures AB, Lund, Sweden

ABSTRACT

Bispecific antibodies continue to represent a growth area for antibody therapeutics, with roughly a third of molecules in clinical development being T-cell engagers that use an anti-CD3 binding arm. CD3 antibodies possessing cross-reactivity with cynomolgus monkey typically recognize a highly electronegative linear epitope at the extreme N-terminus of CD3 epsilon (CD3ε). Such antibodies have high isoelectric points and display problematic polyreactivity (correlated with poor pharmacokinetics for monospecific antibodies). Using insights from the crystal structure of anti-Hu/Cy CD3 antibody ADI-26906 in complex with CD3ε and antibody engineering using a yeast-based platform, we have derived high-affinity CD3 antibody variants with very low polyreactivity and significantly improved biophysical developability. Comparison of these variants with CD3 antibodies in the clinic (as part of bi- or multi-specifics) shows that affinity for CD3 is correlated with polyreactivity. Our engineered CD3 antibodies break this correlation, forming a broad affinity range with no to low polyreactivity. Such antibodies will enable bispecifics with improved pharmacokinetic and safety profiles and suggest engineering solutions that will benefit the large and growing sector of T-cell engagers.

Introduction

Immune-cell engaging bispecific antibodies are a promising class of therapeutics that have shown potential in treating both hematologic and solid tumor malignancies.[1] Simultaneously engaging cytotoxic T cells or natural killer cells and tumor cells via a tumor-associated antigen (TAA), these bispecific antibodies engage immune cells to kill cancerous cells that have evaded the immune system.[2,3] Starting with blinatumomab, the first bispecific T-cell engaging antibody to be approved by the US Food and Drug Administration (FDA) for patient treatment, many bispecific therapeutics are moving toward clinical use and some have more recently been approved in the US and European Union, include the T-cell engagers tebentafusp, teclistamab, and mosunetuzumab.[4–6]

T-cell stimulation is mediated by the T cell receptor (TCR)-CD3 complex with CD3 as the signaling component, where CD3 needs to be cross-linked to facilitate T-cell activation.[7] Stimulation leads to early activation markers CD69 and CD25 being transcriptionally upregulated on the T-cell surface.[8,9] These markers regulate the magnitude of the T cell proliferative response. Stimulation also causes the T cell to release pro-inflammatory cytokines such as IL-2, IFNγ, TNFα/β and others for Th1-biased cells. A growing body of literature suggests that CD3-targeting bispecific antibodies mimic the principles of kinetic segregation rooted in the mechanism of TCR/pMHC-mediated immunological synapse formation.[10,11] The resulting TCR signaling coupled with cross-linking of

cytotoxic CD8+ T-cells to targets cells expressing the TAA arm of the bispecific molecule can redirect cytotoxic effects toward the targeted cells.[10–12]

For a bispecific antibody to be therapeutically effective, it must simultaneously engage the correct effector and target cells to elicit killing and have favorable pharmacokinetic (PK) properties. Numerous assays have been developed to assess developability concerns in antibodies during preclinical development. Such assays include baculovirus particle (BVP) and polyspecificity reagent (PSR) binding, as well as heparin sulfate chromatography, which assesses nonspecific binding, and affinity-capture self-interaction nanoparticle spectroscopy (AC-SINS), which measures propensity for antibody self-interaction.[13–20]

Historically, the terms polyspecificity and polyreactivity have been used interchangeably. Recently, there has been an effort to distinguish between the two such that polyspecificity refers to antibodies displaying "specific" and moderate off-target binding affinity to a discrete number of proteins that are not structurally or functionally related to the intended target antigen.[21] On the other hand, polyreactivity refers to an antibody's ability to bind nonspecifically to many unrelated proteins and lipids with weak affinity. These "sticky" interactions are thought to be encoded by excessive charge or hydrophobic content in the antibody variable fragment (Fv).[22] We believe our PSR assay identifies polyreactivity, as defined this way, and therefore adopt this terminology herein. Through the process of heteroligation, polyreactivity can enhance the

ⓘ Supplemental data for this article can be accessed online at https://doi.org/10.1080/19420862.2023.2189974.

apparent affinity of an antibody to its antigen when the target antigen is proximal to these unrelated off-target species, such as *in vivo* and in cellular contexts.[23] When present, these off-target interactions can reduce favorable PK properties and bioavailability of clinical antibodies. One systematic study found that significantly more antibodies with low PSR (<0.27) and AC-SINS (<11.8 $\Delta\lambda_{max}$) scores have been clinically approved for patient usage, demonstrating the value of these assays in predicting clinical success.[14] These studies highlight the importance of selecting antibodies with favorable properties for development and, when necessary, of engineering lead candidates to meet criteria associated with overall clinical success.

Studies have described a trend in several T-cell engaging bispecific antibodies associating poor PK properties with affinity for CD3, whereby stronger affinity CD3 antibodies are correlated with a shorter serum half-life.[24,25] This trend is problematic because affinity for CD3 affects other properties that contribute to therapeutic efficacy, such as potency, bio-distribution, and toxicity.[25–29] For example, high CD3 affinity is associated with cytokine release syndrome (CRS) and may result in a lack of potency and proper biodistribution.[25,26,28,30] Ideally, the affinity of the CD3 and TAA arms in bispecific T-cell engagers can be tuned to balance these and additional factors to meet therapeutic objectives.

We suspected that correlation between CD3 affinity and many of these unfavorable properties is rooted in the binding mechanism of CD3-directed antibodies. Of CD3-based bispecific antibodies in the clinic with designated World Health Organization (WHO) International Nonproprietary Names (INNs), most contain anti-CD3 sequences that are derivatives of SP34, a cynomolgus (cyno) cross-reactive lineage known to target the N-terminus of CD3ε, which is a highly electronegative region.[31] It is known that electrostatic interactions play a key role in binding interfaces given the relative strength of ionic contacts and the need to energetically overcome de-solvation.[32] A study assessing amino acid contribution to protein–protein binding found that the charged residue Arg is over-represented in interface hotspots of protein–protein complexes.[33] As high-affinity CD3 antibodies that recognize the CD3ε N-terminus are likely to utilize electrostatic interactions, this would be expected to correlate with higher antibody Fv isoelectric point (pI). According to Shehata et al., monoclonal antibodies (mAbs) with pI ≥9.3 are significantly more likely to be polyreactive.[16] We thus hypothesize that an electrostatic binding mechanism is causative for the correlation between affinity for CD3 and elevated polyreactivity in cyno cross-reactive lineages.

We investigated this problem by characterizing PSR binding, self-interaction propensity, and antibody pI for a panel of clinical CD3-binding antibodies and members of a novel cyno cross-reactive CD3ε N-terminus-targeting lineage with a broad affinity range. After confirming that cyno cross-reactive CD3 lineages had significantly higher scores in the measured biophysical developability assays, we investigated the molecular basis of this problem by solving the crystal structure of a representative antigen-binding fragment (Fab) from our novel CD3 lineage bound to a 13-residue N-terminal CD3ε epitope peptide. Beyond revealing the basis for cross-

reactivity to cyno CD3ε, we employed insights gained from the structure to reduce polyreactivity, self-interaction propensity, and net charge in this CD3-binding lineage, while maintaining affinity for CD3. Overall, we demonstrate a novel engineering approach that could benefit T-cell engaging bispecifics, and may be broadly applicable to other therapeutics with polyreactivity concerns.

Results

Clinical CD3-binding antibodies have a positive correlation between polyreactivity and CD3 affinity.

To investigate potential correlations between CD3 binding and biophysical developability properties, we first assessed our novel CD3 lineage along with a set of 27 unique anti-CD3 antibody Fvs derived from clinical and approved bispecific therapeutics as tracked by The Antibody Society as of June 15, 2020 (Table S1).[34] Within this set of anti-CD3 variable sequences, there are many therapeutic formats (see Table S1). However, to facilitate direct comparisons across this heterogenous group of clinical molecules, the variable regions with anti-CD3 specificity were reformatted into the human IgG1 isotype. Nonspecific binding was measured using PSR binding score and the propensity for self-interaction was assessed using AC-SINS.[19,20]

For our novel CD3 lineage, elevated PSR score, and AC-SINS maximum wavelength shift were positively correlated with monovalent affinity to human CD3εδ ($R^2 = 0.82$ and 0.45, respectively; Figure 1a,b, black circles). We observed a similar correlation to cyno CD3εδ ($R^2 = 0.81$ for PSR and $R^2 = 0.42$ for AC-SINS; Figure 1c,d, black circles). Over the entire clinical set, the average PSR and AC-SINS values for cyno cross-reactive anti-CD3 antibodies were 0.57 and 19.9, respectively, while for human CD3-only binders, averages were 0.26 and 9.56 for PSR and AC-SINS, respectively, (Figure 1e,f). On average, the cyno cross-reactive CD3 antibodies tested had significantly higher PSR and AC-SINS scores than the human-specific CD3 antibodies ($p = 0.0062$ and 0.0236, respectively). This result is congruent with our hypothesis that electrostatic interactions are responsible for the correlation between affinity for CD3ε and elevated polyreactivity in cyno cross-reactive antibodies, as the common epitope recognized by most of these lineages is highly electronegative.[35]

Previous studies have shown that antibodies with elevated pIs are more likely to have clearance issues or to display unfavorable developability properties.[16,36–38] One of these studies found that antibody Fvs with elevated theoretical isoelectric points (pI > 9.3) were significantly more likely to display unfavorable developability properties compared to those with pIs <9.3.[16] To confirm this result and to put the CD3 antibodies in context with these previous findings, we compared previously published polyreactivity data for a set of 137 clinical antibodies to their theoretical Fv pIs, bracketing pIs ≥9.3 and <9.3.[14] In line with these previous findings, we observed a significant difference in polyreactivity across the two groups ($p = 0.0008$) (Figure 1g). We then examined the CD3 antibodies for
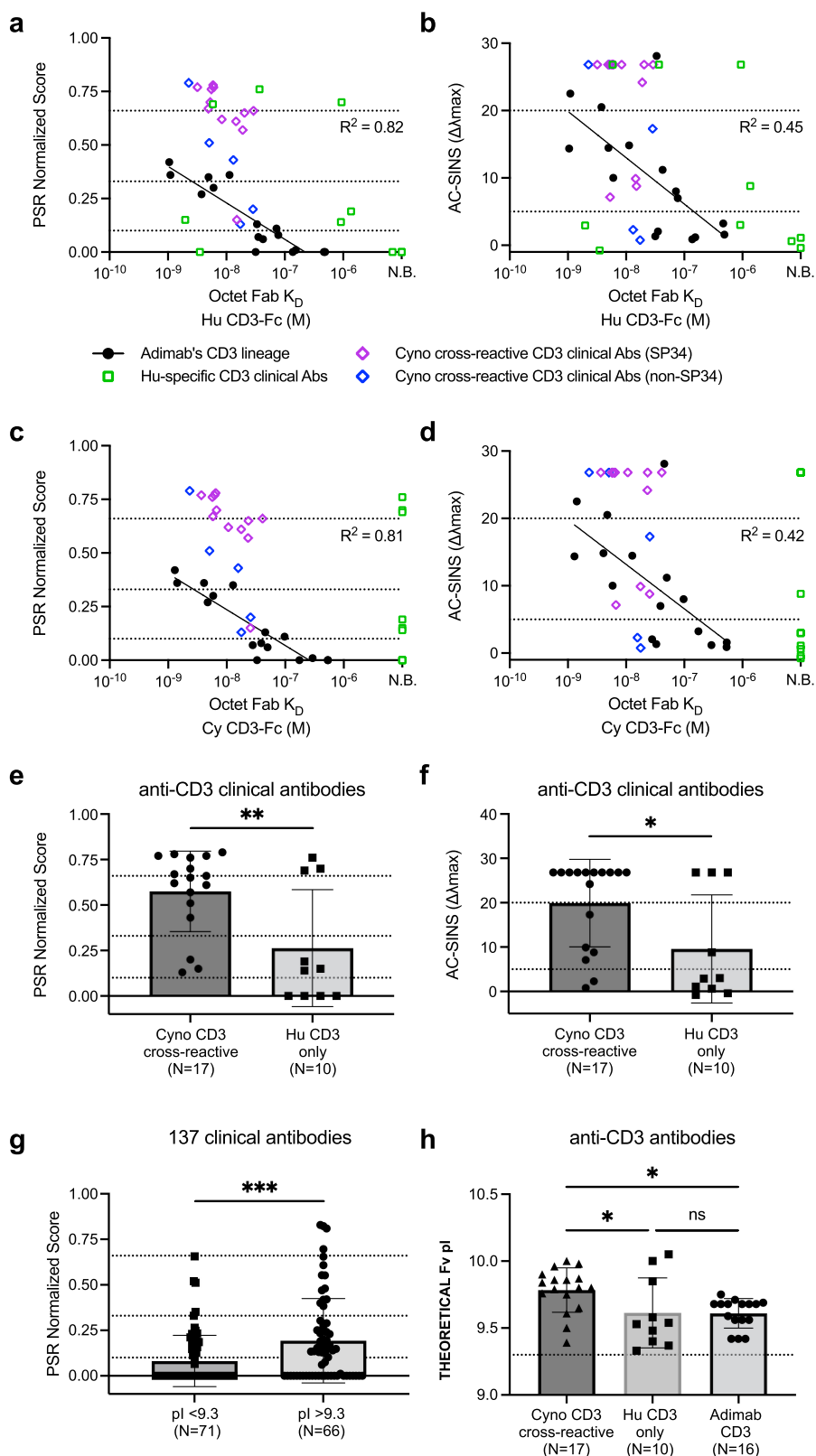
Figure 1. Polyreactivity and affinity are generally correlated for anti-CD3 antibodies. The correlation between (a) polyreactivity and (b) AC-SINS values of anti-CD3 antibodies and monovalent affinity to human CD3εδ. Novel CD3 lineage members are shown as filled black circles. Clinical CD3 antibodies (open symbols) are also plotted, where human-specific CD3 antibodies are shown as green squares and cyno cross-reactive lineages are shown as diamonds, with SP34-derived sequences colored purple and non-SP34-derived colored blue. The correlation between (c) polyreactivity and (d) AC-SINS values of anti-CD3 antibodies and monovalent affinity to cyno CD3εδ, colored and represented as above. A comparison of the (e) polyreactivity and (f) AC-SINS values of clinical CD3 antibodies (not including our CD3 lineage) grouped by cyno CD3 cross-reactivity. A comparison (g) of the polyreactivity of 137 clinical antibodies grouped by theoretical Fv pI < 9.3 (left) and ≥ 9.3 (right). A comparison (h) of the theoretical Fv pI of clinical CD3 antibodies (grouped by cyno CD3 cross-reactivity) and our CD3 lineage. Theoretical Fv pI was calculated using combined variable heavy (VH) and light (VL) sequences. Dashed lines intersecting the Y-axis are included where appropriate for ease of reference for PSR (0.1, 0.33, and 0.66; where low PSR is ≥0.10 and <0.33, medium PSR is ≥0.33 and <0.66, and high PSR is ≥0.66 and ≤1.00), AC-SINS (5 and 20; low is ≥5.0 nm and <20.0 nm and high is ≥20.0 nm) and pI (9.3; where high is ≥9.3). Trendline R^2 values were determined by semi-log linear regression analysis in GraphPad Prism. Statistical analysis was performed with GraphPad Prism using the unpaired t-test, assuming a Gaussian distribution and the same SD for both populations (*$p ≤ 0.05$, **$p ≤ 0.01$ and ***$p ≤ 0.001$).

significant differences in pI across the three anti-CD3 antibody groups. Indeed, the cyno cross-reactive clinical antibody Fvs had a significantly higher pI compared to both the human-only CD3 antibodies and members of our novel CD3 lineage (Figures 1h, S1a). Interestingly, the pI of every clinical anti-CD3 Fv examined was elevated (>9.3), suggesting that in general antibodies targeting CD3 are prone toward more basic pI.

To establish if there was a correlation between affinity and pI, we produced 12 members of our novel CD3 lineage as Fabs and assessed their binding to human CD3εδ by multi-concentration surface plasmon resonance (SPR). Although four of our CD3 antibodies were excluded from the analysis due to having poor fits to a 1:1 binding model at pH 7.4 (Table S2), what data remained demonstrated that stronger affinity antibodies ($K_D \leq 10$ nM) had significantly higher theoretical pI values than the weaker affinity antibodies ($K_D > 10$ nM) ($p = 0.0192$) (Figure S1b). This finding supports our hypothesis that charge interaction contributes to both polyreactivity and affinity as demonstrated by our novel CD3 lineage.

Overall structure of ADI-26906 bound to CD3ε N13 peptide.

To gain structural insight into the recognition of our CD3 antibody lineage, we determined the co-crystal structure of ADI-26906 as a Fab complexed to a 13-residue human CD3ε N-terminal peptide (N13). ADI-26906 is a high-affinity member of our CD3 lineage ($K_D = 1.1 \times 10^{-9}$ M; Table S2) that is also the parental sequence for most lineage members. Thus, we expected that insights gleaned from the structural analysis would be directly applicable to most members. Crystals of the ADI-26906 Fab:N13 peptide co-complex were obtained in space group $P2_1$ and diffracted X-rays to 1.90 Å resolution. A molecular replacement solution was obtained with PHASER using natalizumab Fab as a search model (PBD ID: 4IRZ), where the asymmetric unit (ASU) contained two ADI-26906 Fab:N13 peptide complexes. Iterative rounds of model-building in COOT and refinement in PHENIX produced a final structure with R_{work}/R_{free} of 0.162/0.193 (Table S3).[39–43]

In both biological assemblies present in the ASU, heavy-chain electron density was observed from Glu1 (converted to pyroglutamate; PCA1) to Pro217 (Chothia numbering for variable regions, Eu numbering for constant regions). However, density for a 7-residue region in CH1 (Ser131 to Gly137—end of A-strand into the A-B loop) was missing, likely due to conformational heterogeneity or flexibility. Similarly, in both biological assemblies contained in the ASU, we observed electron density for the human kappa light chain from Asp1 to Arg211, although one kappa chain had electron density extending to Glu213. The interface of the two complexes within the ASU does not disrupt or coincide with either of the equivalent CD3ε N13 peptide-binding sites. With a calculated root-mean-squared deviation (RMSD) of 0.615 Å, there was little difference in atomic coordinates between the two biological assemblies. As such, a single biological assembly will be considered for most of the subsequent structural analysis.

Following iterative refinement and model building, we observed electron density for the first seven residues (QDGNEEM) of the human CD3ε N13 peptide (QDGNEEMGGITQT). A simulated annealing omit map was generated using PHENIX after refinement, which showed high-quality ligand electron density, suggesting that the model was built correctly and free of substantial phase bias (Figure 2a). The extreme N-terminus of CD3ε is ordered and forms a canonical 3_{10} helix (DGNEE residues) that sits in a concave paratope at the binding site of ADI-26906 (Figure 2a,b). Considering slight differences between the two biological assemblies in the ASU, the shape complementarity of this interaction is high – between 0.77 and 0.82 as calculated by *PACKSTAT* in ROSETTA.[44] The ligand primarily engages with residues in complementarity-determining regions (CDRs) H3, L1, and L3, with 20%, 17%, and 25% of the solvent-accessible surface area (SASA) of each respective CDR contacting the peptide. CDRs H1, H2, and L2 make the least contact with the ligand at 5.6%, 4.6%, and 0%, respectively (Figure 2c, Table S4). To our knowledge, this structure represents the first deposition of CD3ε coordinates to include the extreme N-terminus, as this region was unmodelled in previous structures of the CD3ε extracellular domain, including recently solved cryogenic electron microscopy structures of CD3ε-containing TCR complexes.[45–49]

To assess the hypothesis that electrostatics are important for the intermolecular interactions between ADI-26906 and the N13 peptide, we generated electrostatic surface potential maps of both the ligand and the paratope at pH 7.0 using PYMOL and APBS (Figure 2d).[50] We found that the resolved portion of the ligand surface is highly electronegative. The ADI-26906 paratope contains positively charged patches at the paratope – ligand interface, whereas the surface potential of non-paratope regions of the Fv are less positively charged.

Structural determinants of the ADI-26906:CD3ε interaction.

The first residue of the N13 peptide plays a crucial role in the ADI-26906:CD3ε binding interaction. Like the N-terminus of many antibody VH domains, after signal peptide cleavage of the CD3ε pre-protein, the remaining N-terminal glutamine residue spontaneously cyclizes to pyroglutamate under physiological conditions (pGlu1).[51] pGlu1 is buried within a deep pocket at the center of the paratope and makes the most contacts with the paratope. On one side of its binding pocket, pGlu1 makes hydrophobic contacts with aromatic residues H3-Tyr100 and H1-Tyr33 (Figure 2e, upper half). On the other side of its binding pocket, pGlu1 is stabilized by hydrogen bonds with L3-Arg96, H1-His35 and H3-Asp95 (Figure 2e, lower half) while H1-His35 and H2-Trp50 form aromatic pi-stacking interactions with each other that brace the pGlu1 binding pocket (Figure 2e, bottom right).

CD3ε N13 residue Glu6 also plays an important role in binding to ADI-26906. Glu6 is almost completely buried (95%) and its binding pocket is composed of residues in CDR H3 and L1 (Figure 2f). The overall shape of this interaction resembles a hydrophobic molecular pincer formed by the
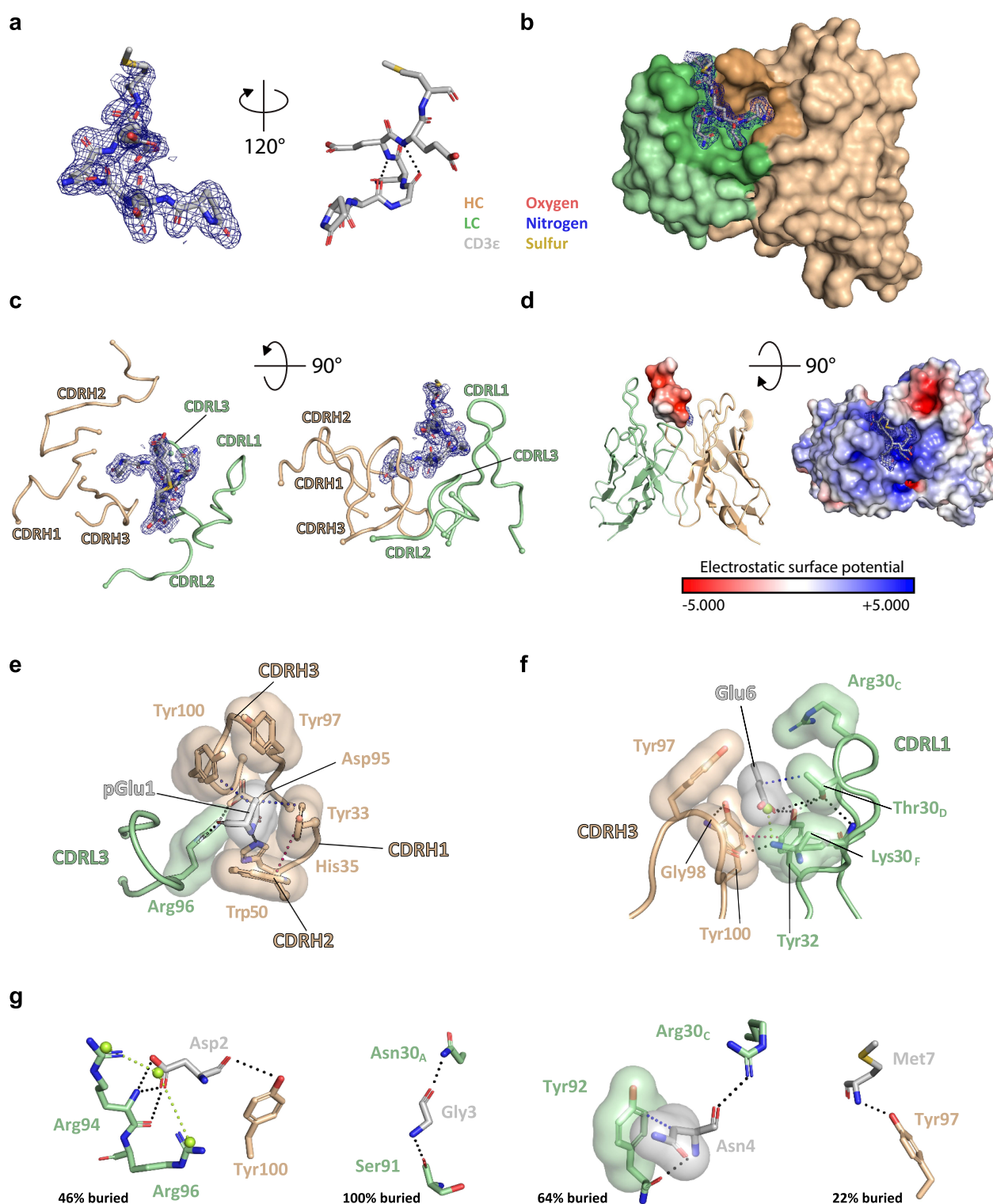
**Figure 2.** The CD3ε peptide is cradled in a concave paratope on the ADI-26906 Fv. Crystal structure of the CD3ε N-terminal peptide bound to ADI-26906 Fab (shown as Fv). (a, b) The CD3ε peptide is shown as a ball-and-stick model, with carbon atoms colored light gray, oxygen atoms red, nitrogen atoms blue and sulfur atoms yellow. The peptide 2Fo-Fc electron density at 3.0 sigma is shown as a blue mesh with a 1.8 Å carve. (a) 2Fo-Fc density was calculated from an SA omit map generated in PHENIX after simulated-annealing refinement with the inhibitor occupancy set to 0.0 and with zero occupancy atoms ignored during refinement. 120° clockwise rotation around the Y-axis of the CD3 peptide is shown with black dashed lines showing the hydrogen bonds that form the canonical 3_{10} helix (b) ADI-26906 Fv is shown as a molecular surface with heavy chain colored tan and light chain colored green, where the binding footprint of the peptide is shown in darker shades. (c) The top and side view of the CD3ε peptide proximite to isolated CDR loops of ADI-26906 which are shown as ribbons. Chains and the CD3 peptide are colored the same as in 2a and 2b (d) The electrostatic surface potential (calculated at pH 7.0 using ABPS) of the CD3ε peptide (left) and the paratope of ADI-26906 Fab (right), are shown as a color scale from red (predicted electronegative surface patches) to blue (predicted electropositive surface patches). Top view (e) of N-terminal pyroglutamic acid of the CD3ε peptide bound to the ADI-26906 paratope. Side chains are shown as transparent molecular surfaces. Key interactions are represented as dotted lines, with hydrophobic interactions in blue, aromatic pi-stacking interactions in pink, hydrogen bonding in gray, and salt bridges in lime green. Top view (f) of Glu6 of the CD3ε peptide bound to the ADI-26906 paratope. Colored the same as 1e. The center-of-charge of the carboxylic acid of glutamate is represented by a spherical pseudoatom colored lime green. Views (g) of Asp2 (leftmost), Gly3 (middle left), Asn4 (middle right), and Met7 (rightmost) residues on the CD3ε peptide and their interactions with key residues in the ADI-26906 paratope, colored and represented the same as in 1f. Residues in the antibody variable regions are referred to using the Chothia numbering system.
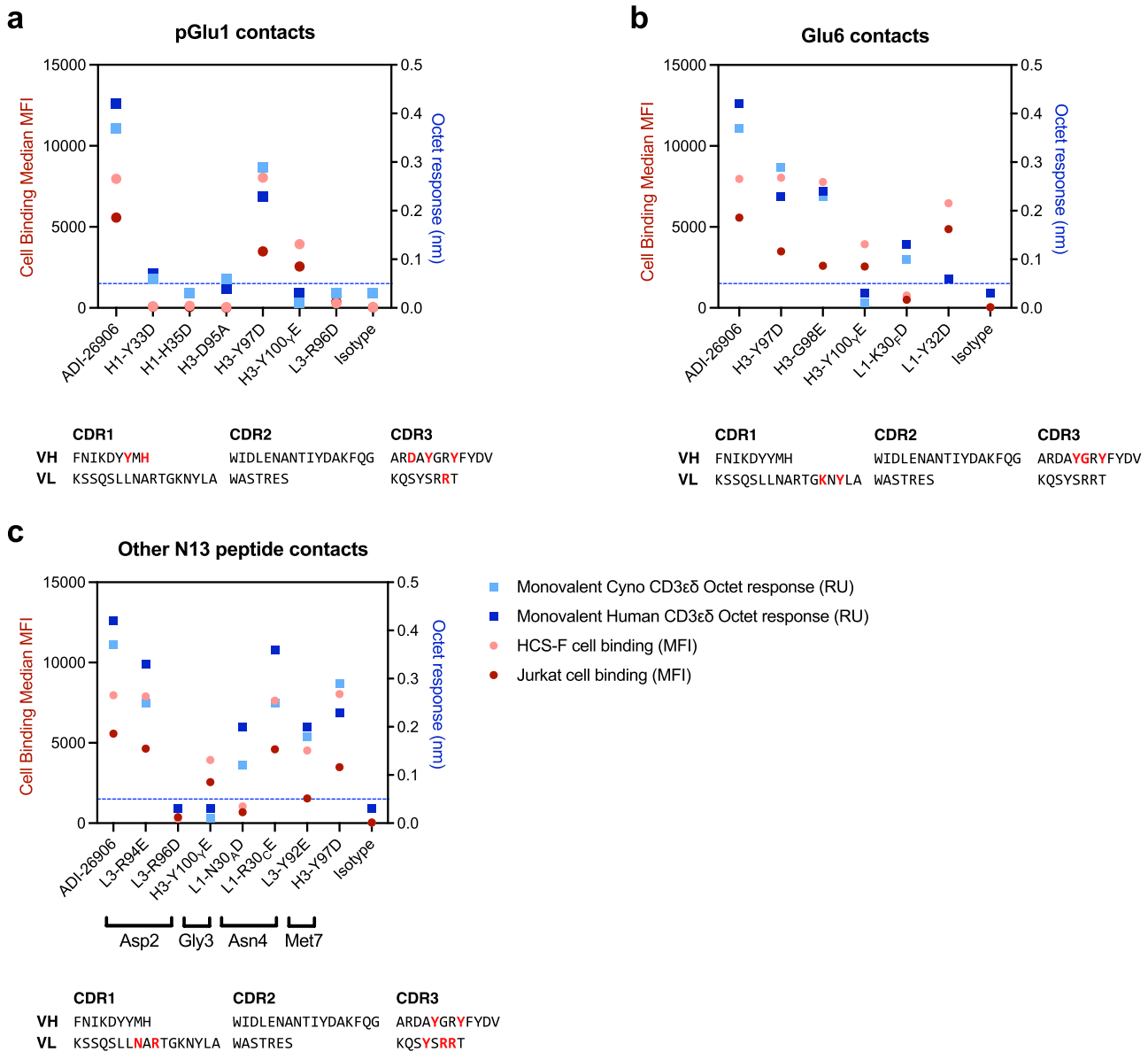
Figure 3. Analysis of single amino acid substituted variants supports insights from the ADI-26906:CD3ε peptide co-complex structure. ADI-26906 IgG binding to cells (left Y-axes) or CD3εδ as assessed by BLI (right Y-axes) when key side chains (highlighted red in sequences) that were identified to interact with either (a) pGlu1, (b) Glu6, (c) Asp2, Gly3, Asn4, or Met7 through crystallographic analysis were substituted. Cell binding MFI is shown in red circles, with the dark red as human Jurkat and light red as cyno HCS-F cells. BLI responses are shown in blue squares, with dark blue as human CD3εδ binding and light blue as cyno CD3εδ binding. ADI-26140, (far right of each graph) the IgG1 isotype control, is included for comparison.

ADI-26906 paratope that clasps Glu6 in a deep groove. An acidic amino acid, Glu6 forms a salt bridge with L1-Lys30$_F$ that tethers it to this binding pocket. A network of hydrogen bonds between Glu6 and its contacting residues L1-Thr30$_D$, L1-Lys30$_F$, and L1-Tyr32 appears to strengthen the overall binding interaction (Figure 2f, right side). Adjacent to this hydrogen bond network, a hydrophobic interaction between the gamma carbon of L1-Thr30$_D$ that aligns with and contacts the beta carbon of Glu6 strengthens the overall binding interaction. On the heavy-chain side of the Glu6 binding pocket, several residues provide structural support to and increase the size of the hydrophobic-binding pocket. There, the H3-Gly98 backbone forms hydrogen bonds with both H3-Tyr100 and L1-Lys30$_F$, and H3-Tyr100 forms an aromatic pi-stacking interaction with L1-Tyr32 (Figure 2f, left side).

Other peptide residues contact the binding site to varying degrees. While Asp2 is only 46% buried, it forms two salt bridges with two adjacent positively charged residues in the CDR L3 (L3-Arg94 and L3-Arg96). Asp2 also forms hydrogen bonds with the peptide backbone between the two Arg residues in the L3 (Figure 2g, left-most panel). These interactions suggest that Asp2 is an important contact for ADI-26906. Gly3 is fully buried in the paratope, and its peptide backbone forms hydrogen bonds with L1-Asn30$_A$ and L3-Ser91 (Figure 2g, middle-left panel). Asn4 is 64% buried and forms hydrogen bonds with L1-Arg30$_C$ and L3-Tyr92 (Figure 2g, middle-right panel). Mostly unburied (22%) and generally free to interact with solvent, Met7 makes a single hydrogen bond contact with H3-Tyr97 via the main chain (Figure 2g, right-most panel).
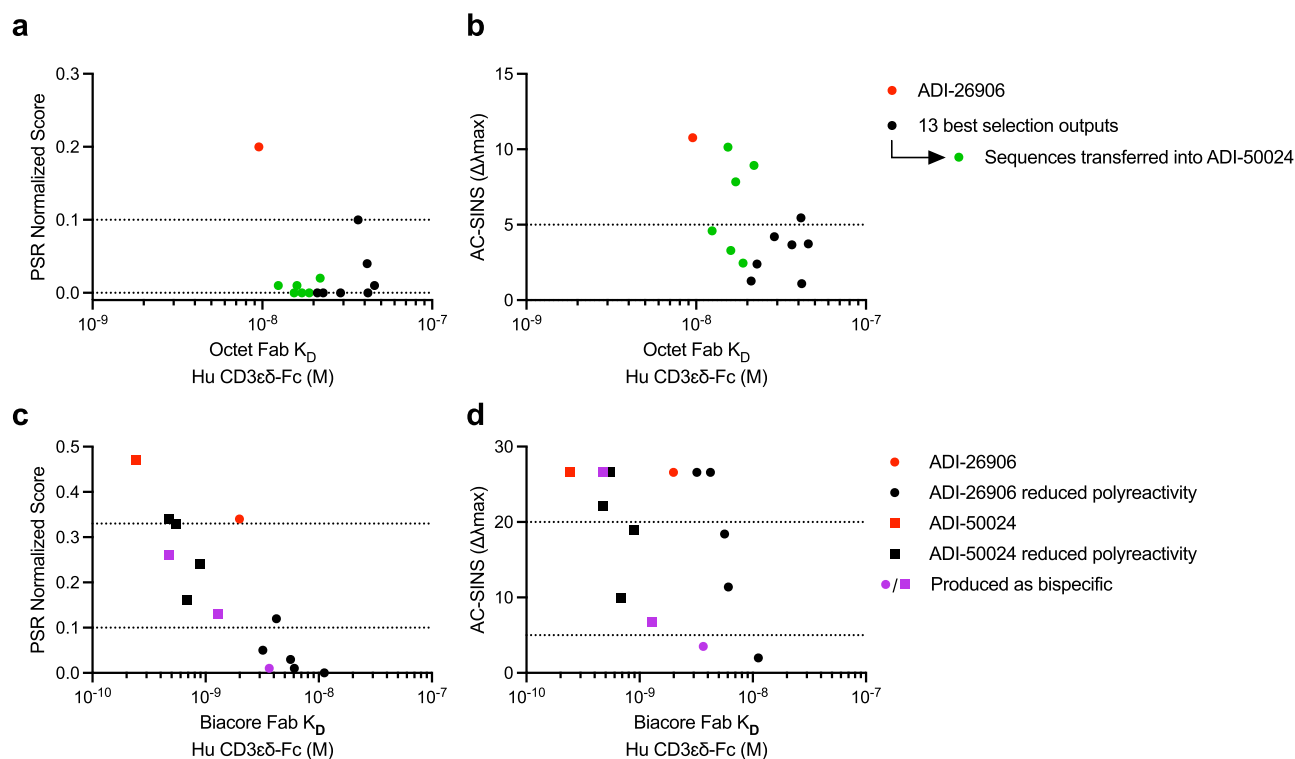
Figure 4. Acidic amino acid substitutions from top outputs decreased polyreactivity when transferred into the sequence of a high affinity lineage member. Human CD3εδ affinity versus the (a) polyreactivity and (b) AC-SINS value of the initial 13 best outputs from our ADI-26906 engineering efforts, in relation to their monovalent affinity to human CD3εδ, shown as filled black or green circles, with ADI-26906 shown as a red circle. Highlighted in green are the clones from which we transferred the acidic amino acid substitutions into ADI-50024, our high affinity CD3-binding variant. Human CD3εδ affinity versus the (c) polyreactivity and (d) AC-SINS value of ADI-26906 and ADI-50024 offspring substituted with the reduced polyreactivity substitutions from the six clones, shown in black or purple. ADI-50024 offspring are shown as squares, with parents shown in red. Highlighted in purple are the clones we chose to validate in a bispecific format. Dashed lines intersecting the Y-axis (panels a – d) are included where appropriate for ease of reference for PSR (y = 0.1 and 0.33; where low PSR is ≥0.10 and <0.33 and medium PSR is ≥0.33 and <0.66) and AC-SINS (y = 5 and 20; low is ≥5.0 nm and <20.0 nm and high is ≥20.0 nm).

Overall, these observations of the molecular determinants underlying the ADI-26906 Fab:CD3ε-N13 complex support the hypothesis that, in addition to shape complementarity and hydrophobic contacts, the binding interaction is strongly driven by electrostatics. As described above, three key salt bridges form at this electrostatic interface: Asp2 on the peptide forms salt bridges with both L3-Arg94 and L3-Arg96, and Glu6 forms a salt bridge with L1-Lys30$_F$. Although Glu5 has the potential to also form a salt bridge, the structure reveals that it is not involved in any distinct molecular interactions and that it barely contacts the paratope (9% buried). Importantly, as the six C-terminal residues of the CD3ε N13 peptide (GGITQT) are unresolved in the structure and presumably do not make appreciable contact with ADI-26906, this demonstrates that the first seven residues (QDGNEEM) of CD3ε are sufficient for the interaction. As the published sequence of cyno CD3ε N-terminus (Uniprot: Q95LI5) is identical to human (Uniprot: P07766) in this region, our structure confirms that this shared stretch of amino acids is the basis for the cyno cross-reactivity of ADI-26906.

Structure-based rationale for reducing polyreactivity in our novel CD3 lineage.

With knowledge of the ADI-26906:CD3ε binding interface and, importantly, positions within ADI-26906 that may be amenable to substitution without disrupting CD3ε binding, we sought to engineer ADI-26906 to decrease its polyreactivity while maintaining the overall strength of CD3ε binding. To counter the positively charged binding surface and decrease the overall antibody Fv pI, we introduced acidic amino acid substitutions into CDRs of ADI-26906. Based on the structure, we anticipated that CDRs H1, H2, and L2 would be the most productive sites for incorporation of acidic amino acids; specifically, solvent-exposed positions distal from the antigen-binding interface. CDR H2 is the longest of the three candidate CDRs, with 17 residues. Its SASA makes up nearly a quarter of the total SASA of all CDRs in ADI-26906 (Table S4). Thus, we predict that there should be many positions along H2 that can serve as beneficial substitution sites.

To implement this structure-guided engineering approach, we built antibody libraries of diversified ADI-26906 heavy and light chain CDRs. In total, we created 14 acidic amino acid substitution libraries (7 per chain) and pooled by mutational load to three final libraries for selection and screening (Figure S2). Each of the three libraries introduced intrachain-only substitutions: either one, two, or three acidic amino acid substitutions to the CDRs of the ADI-26906 heavy or light chain. To avoid over-diversifying ADI-26906, combinatorial interchain substitutions across the heavy and light chain were excluded from the design.

Single aspartic and glutamic acid substitutions validate structural findings.

We used members of the single acidic amino acid substitution library to validate our structural findings. This involved isolating all unique ADI-26906 variants that had either an Asp or Glu substitution at each heavy and light chain CDR position. Alternatively, positions in parental ADI-26906 CDRs already containing Asp or Glu were substituted with alanine. We then characterized this collection of single substitution variants to assess which CDR residues had the most profound impact on the ADI-26906:CD3ε interaction (Figure 3a-c).

Overall, the cell staining and biolayer interferometry (BLI) binding results agreed with the structural findings and provided insight into the relative importance of each residue at the binding site. Notably, almost a complete loss of binding was observed for many of the pGlu1-contacting residues, validating that pGlu1 interactions are crucial to the overall ADI-26906 interaction with CD3ε (Figure 3a).

This dataset also validated the importance of the electrostatic interactions at the binding site. The charge-swap substitution L1-K30$_F$D knocked out binding to CD3 on T cells through disruption of a putative salt bridge formed between Glu6 and L1-Lys30$_F$ (Figure 3b). Similarly, the L3-R96D substitution disrupts binding to human and cyno recombinant CD3εδ protein and T cells through the loss of a putative Asp2-contacting salt bridge (Figure 3c). Interestingly, the L3-R94E charge swap substitution only moderately impacted CD3ε binding, suggesting that the L3-Arg94:Asp2 salt bridge is the least important present at the ADI-26906:CD3ε binding interface.

Acidic amino acid substitutions successfully reduced polyreactivity in ADI-26906 and high-affinity variant ADI-50024.

Using the three pooled libraries described above, we performed three rounds of selections to identify antibodies that maintain CD3 affinity with reduced polyreactivity (Figure S3). In the first round, libraries were incubated with 100 nM CD3εδ heterodimer and clones with binding comparable to parental ADI-26906 were sorted (Figure S3, leftmost panels). The CD3εδ heterodimeric antigen is composed of the CD3ε extracellular domain fused to an Fc and the CD3δ extracellular domain fused to another Fc with a C-terminal His tag using knob-into-holes-like technology.[46] In the second round, we sorted clones that did not bind PSR (Figure S3, middle panels). In the third round, we labeled the round 2 output at a range of CD3ε N13 peptide concentrations (1, 10, 100 nM) and sorted clones with binding equal to or better than ADI-26906 (Fig S3, rightmost panels). From the output of the third round, 20–40 clones from each library were down-selected after testing for improved polyreactivity profiles while still maintaining near-parental levels of binding to CD3 as assessed by human and cyno T cell staining and BLI binding of recombinant human and cyno CD3εδ heterodimer.

Our toggling selection strategy yielded 13 promising clones that fell within the following criteria:

- Within 2-fold of parental Hu CD3εδ K$_D$ by BLI
- Within 2-fold of parental Cyno CD3εδ K$_D$ by BLI
- Within 1.25-fold of parental Hu CD3εδ response by BLI
- Within 1.25-fold of parental Cyno CD3εδ response by BLI
- Within 2-fold of parental Hu CD3+ cell binding MFI (100 nM IgG)
- Within 2-fold of parental Cyno CD3+ cell binding MFI (100 nM IgG)
- >2-fold reduction in PSR binding as compared to ADI-26906

We repeated the characterization of these 13 clones with a wider set of assays, including AC-SINS and Fab binding via BLI to CD3εδ.[20] In general, these matured variants had greatly reduced PSR and AC-SINS scores compared to ADI-26906, with limited reductions in CD3εδ affinity (Figures 4a,b).

We wanted to test if the same acidic amino acid substitutions could lower polyreactivity in a high affinity variant of ADI-26906. To do so, we first selected six variants, chosen based on greatest reduction in AC-SINS and PSR and maintenance (within 0.7-fold) of monovalent binding BLI response to both human and cyno CD3εδ (Figure 4a,b). All six clones had sequences with acidic amino acid substitutions exclusively in CDRs H1 and H2, except for ADI-67445 (Table S5). This outcome matched the structure-guided prediction that CDRs making the least contact with CD3ε would be the most productive sites to include acidic amino acid substitutions.

We introduced the acidic amino acid substitution combinations into the sequence of ADI-50024 (Table S5). ADI-50024 is an ultra-high affinity variant of ADI-26906 (59 pM toward human CD3εδ-Fc as assessed by Fab on SPR; Table S2) with, consequently, higher polyreactivity (Figure 4c). For the single clone that had a substitution outside of H1 or H2 (ADI-67445), we omitted the substitution in its CDR H3 (V102E) when incorporating into ADI-50024 (Table S5) based on our structure-guided rationale. Following IgG and Fab production in Chinese hamster ovary (CHO) cells, we characterized these antibodies, observing that these substitution sets successfully lowered polyreactivity, self-interaction, and, as expected, predicted pI in the context of ADI-50024 (Figure 4c,d; Figure S4a; Table S5; Table S6). These substitutions had a markedly similar effect in ADI-50024 as in ADI-26906, lowering polyreactivity while having a modest effect on affinity. Interestingly, the observed reduction in affinities compared to the parental Fabs (Figure 4c,d; Table S6) are due to reduced rates of association (k_{on}) rather than reduced rates of dissociation (k_{off}). This is especially the case for ADI-50024 and its substituted offspring (Figure S4b).

While there remains a trend between polyreactivity and affinity in the substituted offspring, these IgGs have substantially reduced PSR compared to the parental CD3 antibodies. Indeed, several of the ADI-50024 offspring were found to have comparable or improved affinity to ADI-26906, with considerably reduced polyreactivity and limited effect on thermal stability (Figure 4c,d; Table S6; Figure S4c). Thus, through a structure-guided and an acidic amino acid substitution library and selection approach, we engineered antibodies with comparable
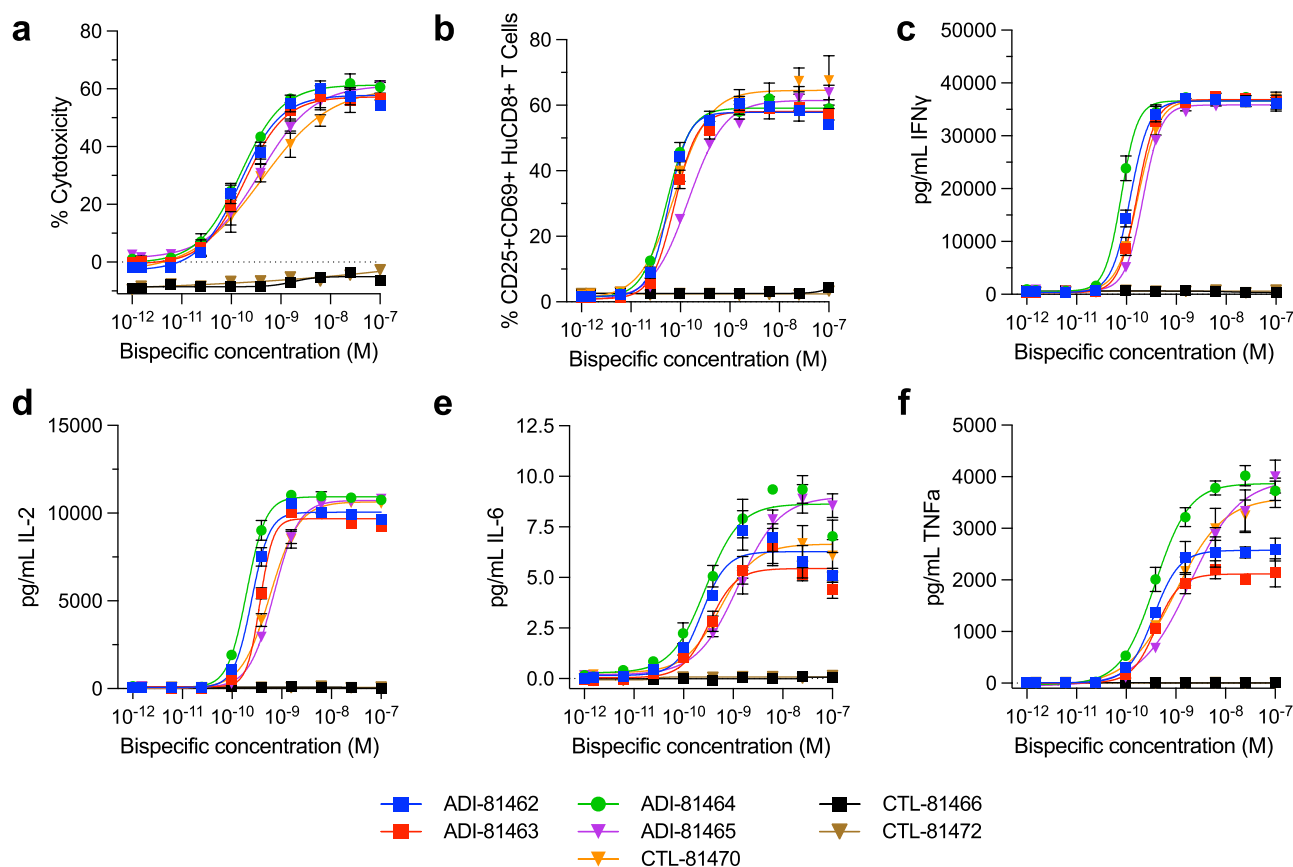
Figure 5. CD20xCD3 bispecific antibodies mediate RTCC *in-vitro*. Preactivated human CD8+ lymphocytes were incubated with serial dilutions of CD20 × CD3 or control bispecific antibodies and CD20-positive Raji cells at an effector:target ratio of 10:1 for 24 h. Flow cytometric analysis was performed to simultaneously evaluate the number of surviving Raji cells (a) as a measure of cytotoxicity and CD8+ T cell activation and (b) by assessing co-expression of CD69 and CD25 activation markers. Cytokine analysis of culture supernatants was performed by multiplexed MSD assays to assess levels of bispecific antibody mediated secretion of IFNγ (c), IL-2 (d), IL-6 (e) and TNFa (f). Data are representative of one experiment with three replicates using lymphocytes from a single human donor.

affinity to our original anti-CD3 antibody lineages, but with substantially reduced polyreactivity properties.

CD3 Fvs with reduced polyreactivity bind native TCR/CD3 complexes on human and cyno T cells.

To confirm the ability of these antibodies to bind native TCR/ CD3 complexes on the surface of immortalized human and non-human primate (NHP) T cells, flow cytometric analysis was performed by incubating three-fold Fab titrations from 100 nM on human Jurkat T cells (Figure S4d, S4e) or the NHP T cell line HSC-F (Figure S4f, S4g). We observed that CD3 Fvs with reduced polyreactivity exhibit titratable binding on Jurkat and NHP cells as Fabs. As expected, based on the Fab SPR analysis that demonstrated reduced on-rates associated with the reduced polyreactivity substituted Fvs (Fig S4b), the parental molecules (ADI-26906 or ADI-50024) had the strongest staining toward both cell lines. Also, in line with expectations, the substitution sets behaved similarly in both parental backgrounds and were generally correlated with their affinity rank (Figure S4d – g, Table S5). These data demonstrate that the recombinant antigens used in engineering efforts to reduce polyreactivity sufficiently recapitulated the native antigens present on immortalized cell lines.

Reduced polyreactivity CD3 Fvs paired as CD20 bispecifics activate T-cells in an antigen-dependent manner.

After demonstrating T-cell activation with the monospecific CD3 IgGs (Figure S5), we sought to benchmark the newly engineered CD3 antibodies as CD20 bispecifics. Variable regions for three of the polyreactivity-engineered CD3 antibodies (ADI-70326, ADI-70327, ADI-67450) were chosen to be reformatted as CD20/CD3 IgG-like, 1 + 1 valency bispecifics, (with the mosunetuzumab anti-CD20 Fv, i.e., ocrelizumab's Fv) because they represented a range of CD3 monovalent affinities (Figure S6a, Table S7). The mosunetuzumab CD3 variable regions were also reformatted into the same Fc-silenced IgG-like bispecific construct, as was a member of our original CD3 panel (ADI-26919) that did not have elevated PSR or AC-SINS (data not shown) yet had similar monovalent affinity toward Hu and Cy CD3εδ heterodimer as mosunetuzumab (Figure S6a, Table S7). Control bispecifics were also produced, where either the CD3 arm or the CD20 arm (mosunetuzumab/ocrelizumab Fv) of the bispecific was substituted with the Fv of a hen egg lysozyme (HEL) binding control antibody, ADI-47926 (Figure S6b). Calculated IgG pIs for three potential IgG-like products for each bispecific construct are shown in Figure S6c. All products were easily separated by our ion-exchange chromatography (IEX) protocol to yield the pure heterodimeric bispecific species.

We first tested the polyreactivity profiles of the bispecific molecules. The PSR normalized scores for the bispecific constructs were clean-to-low (Figure S6d), whereas several of the AC-SINS $\Delta\lambda_{max}$ values were somewhat elevated for experimental, but not the control bispecifics (Figure S6e). Interestingly, for the strongest CD3 affinity bispecifics (whose CD3 Fvs were optimized to reduce polyreactivity), there appears to be a positive trend between affinity and AC-SINS. Whether these are paired with the mosunetuzumab CD20 Fv or with the ADI-47926 HEL Fv determines the magnitude of the $\Delta\lambda_{max}$ signal (higher and lower self-interaction, respectively), though the values are only elevated when paired with the mosunetuzumab CD20 Fv, not with the HEL Fv. On the other hand, the mosunetuzumab and ADI-26919 CD20/CD3 bispecifics both have self-interaction propensities of similar magnitude as ADI-81462, even though they have CD3 Fv affinities far lower than this ultra-high affinity CD3 Fv (Table S7).

Having assessed their polyreactivity profiles, we sought to evaluate the ability of these bispecifics to stimulate T cells through simultaneous engagement of CD20 and CD3 in an NFAT luciferase reporter co-culture assay. For all experimental molecules, a dose-dependent activation of T cells was observed. The mosunetuzumab control, CTL-81470, also activated T cells, while for CTL-81466, which is analogous to ADI-81462 but includes an anti-HEL Fv rather than an anti-CD20 Fv (Figure S6b), no activation was observed at any of the concentrations tested (Figure S6f). EC_{50} of activation for the experimental constructs and CTL-81470 ranged from 57 to 110 pM (Figure S6g). Rank order for activation potency of the molecules could only be partially determined, as only the lower potency of ADI-81465 could be clearly differentiated from the other four molecules, which appeared to be of roughly equal potency based on 95% confidence intervals of the EC_{50} values (Figure S6g). These results demonstrate that the CD20/CD3 bispecifics containing the engineered polyreactivity-reduced Fvs simultaneously bind target and effector cells to activate T cells in a CD20-dependent manner with similar potency as CTL-81470 (mosunetuzumab).

CD3 bispecifics RTCC of activated CD8+ T cells toward Raji cells.

We further benchmarked these bispecific molecules against CTL-81470 in a redirected T cell cytotoxicity (RTCC) assay using primary CD8+ and CD45RA+ cytotoxic T cells, to assay the ability of these molecules to trigger T cell-mediated target-dependent lysis of CD20+ Raji lymphoma cells. At the 24 h timepoint (10:1, E:T) of the cytotoxicity assay, we observed that activated human T cells lysed the CD20-expressing Raji cells (Figure 5a). Lymphoma cell lysis was observed at low picomolar concentrations with EC_{50} values ranging from 150 to 189 pM for bispecifics containing the high affinity reduced polyreactivity novel CD3 Fvs, and 388–412 pM for the low-affinity ADI-81465 and the control molecule containing the mosunetuzumab Fv (CTL-81470) (Figure S7g). Similar cytotoxicity was observed at the 48 h (2:1, E:T) endpoint (Figure S7a). The 48 h endpoint did not appear to be as sensitive, as

calculated EC_{50} values (ranging from 306 to 1220 pM) tended to have wider 95% confidence intervals than the 24 h endpoint assay (compare Figure S7g and S7h). Cytotoxicity at both 24 and 48 h endpoints was accompanied by the induction of activation markers CD69 and CD25 on CD2+ primary T-cells, with EC_{50} values ranging from 50 to 145 pM for the bispecifics incorporating both CD20 and CD3 Fvs (Figure 5b, S7b).

In addition to probing for cytotoxicity and early activation markers, supernatants from both 24 and 48 h endpoint assays were analyzed for the presence of IFNγ, IL-2, IL-6 and TNFα cytokines using the MSD instrument. In all cases where bispecifics incorporated both a CD20 and CD3 Fv, there was detectable cytokine secretion at low picomolar levels and clear dose dependence where EC_{50} ranged from 78 to 405 pM for IFNγ, 197–1390 pM for IL-2, 231–1480 pM for IL-6 and 317–1950 pM for TNFα (Figure 5c-f, Figure S7c – f). Importantly, the lack of substantial signals from the titration of our CD20 and CD3 arm control bispecifics (CTL-81446 and CTL-81472, respectively) demonstrate that dual engagement of CD20 and CD3 is required to mediate not only the observed cytotoxic effects, but cytokine release as well (Figure 5, S7). In general, we observed that higher ratios of effector cells elicited more pro-inflammatory cytokines in the supernatant (compare Figure 5 and S7) and that molecules containing Fvs with strong CD3 affinity generally resulted in higher levels of cytotoxicity than those with weaker CD3 affinities, as expected based on what has been previously reported in the literature.[28,49] Together, these data demonstrate that, in an RTCC assay, our reduced polyreactivity engineered CD3 Fvs activate T cells to secrete pro-inflammatory cytokines and kill CD20-expressing lymphoma cells in a CD20/CD3 bispecific format with comparable efficacy as the CTL-81470 (mosunetuzumab) control.

Discussion

In this study, we investigated the mechanism underlying the link between CD3 binding and polyreactivity in clinical CD3 antibodies, as well as in our unique CD3 lineage. We first established that clinical CD3 antibodies, especially the cyno cross-reactive lineages, have elevated PSR, AC-SINS values, and Fv pI. Specifically, we observed a strong correlation between these developability properties and CD3 affinity in our unique lineage. These results are congruent with several studies showing that CD3 affinity in the context of T-cell engaging bispecific antibodies has been associated with poor PK.[26,52] These findings are also harmonious with literature assessing the utility of such developability properties in predicting the PK and safety profiles of therapeutics in the preclinical stage.[14,16]

With the solution of the ADI-26906 Fab:N13 CD3ε peptide co-complex structure, we confirmed that this lineage binds to an electronegative region on CD3ε that is conserved in cynomolgus monkey. The CD3ε N-terminus present in the structure is post-translationally modified to pyroglutamic acid and electrostatic interactions play an important role in the formation of the complex. Our characterization of ADI-26906's

binding mechanism is congruent with studies demonstrating that electrostatic interactions play an important role at protein–protein binding interfaces. Studying protein–protein interfaces, Bogan et al. found that Arg residues are overrepresented in binding interface hot spots.[33] However, the positioning of charged residues at the binding interface is critical. To energetically favor binding, intermolecular pairs of charged residues at the binding interface need to be positioned precisely to form salt bridges. Otherwise, these charged residues will contribute substantially to nonspecific binding and self-interaction.[53] For example, a study by Sidhu et al., compared the binding contributions of Tyr, Ser, Gly and Arg in antibody CDRs and found that Arg was enriched in weaker affinity clones with higher levels of nonspecific binding.[54]

To ensure correct positioning, charged residues are typically incorporated into CDRs during affinity maturation to fine-tune naïve interactions.[55] Since charge patches can contribute to polyreactivity, it is important to assess the contribution of a charged residue to the specificity of binding. In analyzing the crystal structure of ADI-26906, we observed that positively charged residues in the Fv substantially contribute to CD3ε binding affinity. These amino acids are positioned optimally in the binding site to form intermolecular salt bridges to support the binding interaction. This finding is unsurprising given that ADI-26906 has undergone both somatic hypermutation and many iterations of affinity maturation. However, this also suggests that affinity to CD3 and polyreactivity are intrinsically linked in cyno cross-reactive lineages, including ADI-26906, its lineage members, and very likely the SP34 and mosunetuzumab lineages, as the structural information provided by the published patents on these molecules suggest that the binding mode is highly similar to the ADI-26906-CD3ε interaction and that they target the same electronegative N-terminal CD3ε peptide.[35]

In our analysis, we observed the same linkage between CD3 affinity and polyreactivity in cyno cross-reactive clinical CD3 antibodies. One limitation was that these clinical cyno cross-reactive CD3 lineages have a narrow affinity range. In contrast, our CD3 lineage has many members spanning roughly 2–3 orders of magnitude of CD3 affinity, thus the *correlation* between polyreactivity and affinity is clear. However, high polyreactivity was a clear *property* in non-SP34 lineage members as well as in the SP34 lineage, apart from a single Fv sequence outlier that had low polyreactivity (Figure 1a, b). This clone, GBR1302, is unique among the SP34 lineage, as it was humanized in the context of a V-kappa template rather than the more typical V-lambda. Humanization on the V-kappa template reduces the overall pI of the GBR1302 Fv, reducing its propensity toward polyreactivity.

As complete removal of the positively charged residues from our CD3 lineage would be difficult due to their demonstrated importance in binding (Figure 3), we instead chose to counterbalance elevated antibody pI by performing unbiased acidic amino acid scanning using directed evolution and selection pressures. We hypothesized that adding negatively charged amino acids in CDRs with limited antigen contact would balance the positive surface patches in the binding region and help to decrease the polyreactivity of the Fv. This strategy was successful and, as predicted through structural

analysis, the offspring with the most improved polyreactivity had acidic amino acid substitutions predominantly in CDRs with the least contact to the N13 peptide. These specific substitution combinations were directly translatable to other members of the ADI-26906 lineage, including a high-affinity antibody, ADI-50024, with elevated polyreactivity. This finding was unsurprising given that we had initially chosen ADI-26906 for structural analysis because it was the parent of many lineage members. We expected the overall binding mode to remain generally consistent in its offspring, thus we suspected that productive acidic amino acid substitutions could be imported into ADI-26906 lineage members without a substantial effect on affinity. Although solution of the ADI-26906 Fab:N13 CD3ε peptide co-complex structure yielded both important insights into the mechanism underlying the linkage between polyreactivity and antigen binding, and correct predictions as to which CDRs would be the most successful to apply acidic amino acid scanning to, our engineering strategy was performed independently and was unbiased by the structural information.

While at a broad level, lowering pI was able to reduce polyreactivity in members of our CD3 lineage with minimal reduction in affinity, we did observe a small yet concurrent reduction in CD3 affinity to the substituted variants. Interestingly, this effect is almost solely the result of a decreased on-rate (Figure S4b). Previous studies have demonstrated that electrostatic interactions are strongly correlated with the rate of association and that long-range attractive charge interactions are dominant factors in the kinetics of protein-protein association.[56] The sum of electrostatic interactions of two interacting molecules (i.e., the difference in pI between two molecules) likely serves as an initial long-range steering force that brings two molecules in proximity of each other before other forces, like hydrogen bonds and shape complementarity, can play a role. Indeed, simulations and empirical studies have demonstrated that electrostatic steering forces can be modulated to increase association rates while leaving dissociation kinetics unchanged.[57,58] In our study, with reduced basic electrostatic surface potentials, acidic amino acid-substituted offspring of our CD3 lineage likely have a reduced net attraction to molecules with strong acidic surface potential resulting in the observed reduced association rates.

By employing the methods described herein, we created a panel of CD3 binders at various affinities that have uniformly low polyreactivity. Having a range of CD3 affinities to test during preclinical development is beneficial as CD3 affinity has been shown to modulate a host of properties, such as T-cell activation potency, biodistribution, and CRS toxicity. For example, higher CD3 affinity has been found to be advantageous in the context of a bispecific antibody with the TAA arm targeting a low-density receptor.[25] However, drawbacks of higher CD3 affinity include higher likelihood of CRS and biodistribution to T cell-rich sites away from the tumor. By breaking the strong correlation between polyreactivity and CD3 affinity, we have likely down-weighted PK in this complex equation.

It can also be argued that heteroligation could contribute to CRS due to the elevated polyreactivity seen in most clinical anti-CD3 antibodies, including known bad actors, such as muromonab, which has a product label that

includes a black box warning for CRS.[59] Certain infectious agents, including the Epstein-Barr, hepatitis C, and human immunodeficiency viruses, cause the human immune system to produce polyreactive antibodies that are capable of bivalent heteroligation that increases their apparent affinity to the target antigen.[23] Given the elevated polyreactivity of most clinical anti-CD3 antibodies, it is possible that the same mechanism could occur when these antibodies bind to the CD3 antigens expressed on the surface of T cells. Heteroligation of polyreactive anti-CD3 variable regions could result in an increase in their apparent affinity to T cell-associated CD3, potentially leading to an overactive immune response and the release of large amounts of cytokines, a hallmark of CRS.

Although the findings are clear, our method of reformatting the anti-CD3 variable regions into IgG1s, while allowing us to compare to a vast amount of data and to apply standards based on that data, represents a limitation of our investigation because the final therapeutic format of these molecules may change their overall polyreactivity profiles. Indeed, this was observed upon reformatting the polyreactivity-optimized variants into CD20 × CD3 1 + 1 IgG-like bispecifics, and associated controls. While PSR scores were modest for our set of bispecifics, there was a trend observed in the AC-SINS $\Delta\lambda_{max}$ values for ADI-70326, 70327, and 67,450 (Fig S6a, b). When paired with the mosunetuzumab CD20 arm, these bispecifics demonstrated elevated AC-SINS values corresponding to their CD3 affinity (Table S7), while when paired with HEL-binding control antibody, ADI-47926, AC-SINS values were substantially reduced, though still correlated to CD3 affinity. While mosunetuzumab has elevated polyreactivity compared to ADI-47926 when produced in CHO as IgG1 monospecifics, the trends are not clear enough to be of predictive value (data not shown). This suggests that, while it is important to monitor and engineer polyreactivity of the components of a bispecific molecule, an assessment of these biophysical properties in the final therapeutic format is critical.

Overall, we demonstrated that acidic amino acid substitution can be an effective way to lower polyreactivity in therapeutic proteins that rely on electrostatic-binding interactions and have high pIs. Previous studies have used acidic amino acid scanning of CDRs as a general strategy to increase antibody aggregation resistance, typically caused by enrichment of hydrophobic residues.[60,61] As with the work shown here, these studies indicated that placement of these acidic residues must occur in positions that do not interfere with cognate antibody–antigen interactions and that solvent exposure of the residues is important for their effect. Although untested by us, this concept should also hold in the other direction of charge, where basic amino acid substitutions can be used for polyreactive therapeutics molecules with low pIs. This method can potentially be used to improve PK-modulating properties of not only other T-cell engaging bispecific antibodies, but any therapeutic with elevated polyreactivity and a charge-dependent binding mechanism.

Materials and methods

Cell lines

Human Jurkat Clone E6–1 suspension cells were obtained from American Type Culture Collection (ATCC, #TIB-152) and grown in RPMI-1640 (Corning/CellGro) supplemented with 10% fetal bovine serum (FBS; BioWest). CD3-negative Jurkat suspension cells (J.RT3-T3.5) were obtained from ATCC (#TIB-153) and grown in RPMI-1640 supplemented with 20% FBS. Cyno macaque suspension T cells (HSC-F) were obtained from the NIH Nonhuman Primate Reagent Resource (NHPRR) and grown in RPMI-1640 supplemented with 20% FBS, 20% NCTC-109 (Gibco), 5 mM L-glutamine (Sigma-Aldrich), 1 mM HEPES (Sigma-Aldrich), 1× nonessential amino acids (Corning/CellGro), and 55 nM 2-mercaptoethanol (Sigma-Aldrich). Cells were grown in a humidified 5% CO_2 stationary incubator at 37°C, and 1% penicillin-streptomycin (Corning/CellGro) was used to reduce contamination risk.

Human Burkitt lymphoma Raji cells were procured from Leibniz Institute DSMZ-German Collection of Microorganisms and Cell Cultures GmbH, Germany (#ACC 319) and grown following vendor recommendations. Jurkat NFAT-Luc2 cells were purchased from Promega (#J1625). Naïve primary human CD8+ T cells expanded for the RTCC assay were purchased from StemCell Technologies (#70030).

Expression and purification of IgGs and Fab fragments

Antibodies used for binding experiments were produced as full-length immunoglobulin G1 (IgG1) proteins in *S. cerevisiae* cultures, as previously described.[62] In brief, yeast cultures were incubated in 24-well plates at 30°C, 80% relative humidity with shaking in Infors Multitron shakers. After 6 d of growth, the culture supernatants were harvested by centrifugation, and IgGs were purified by protein A affinity chromatography. Bound IgGs were eluted with 200 mM acetic acid with 50 mM NaCl (pH 3.5) and neutralized with 1/8 (v/v) 2 M HEPES (pH 9.0).

To generate Fabs for kinetics, Protein A (ProA)-purified IgGs were digested with papain overnight at 30°C, followed by an additional dose of papain and 2 h incubation the next day. Iodoacetamide was added to terminate the papain reaction prior to passing the mixture over ProA agarose, removing constant fragment (Fc) and undigested IgG. The flow-through from the ProA resin was passed over the KappaSelect resin (Cytiva, catalog no. 17545803) or LambdaFabSelect resin (Cytiva, catalog no.17548203) for antibodies with the κ or λ light chains, respectively. The KappaSelect or LambdaFabSelect was washed two times with phosphate-buffered saline (PBS) (pH 7.4), then the Fabs were eluted using 200 mM acetic acid with 50 mM NaCl (pH 2.0) into 1/8 [v/v] 2 M HEPES (pH 8.0).

For the antibodies produced by transient transfection in CHO suspension cells, two plasmids encoding the full heavy and light chains were transiently co-transfected at a 1:1 ratio using PEIpro (Polyplus #115–100). Transfected cells were initially grown in 37°C, 8% CO2 incubator, shaking at

130 rpm, then after 24 h, they were transferred to conditions of 32°C, 5% CO2 incubator, shaking at 130 rpm, and given mammalian production feed medium (2% v/v) supplemented with valproic acid (1 mM) and anti-clumping reagent (Irvine Scientific #91150). After 4 and 7 d of growth, mammalian production feed medium was given to cells again (4% v/v), and after 9 d, supernatant was harvested and purified using a ProA affinity column. Fab was generated using an overnight papain digest, followed by a CH1-resin purification step.

To generate ADI-26906 Fab for crystallographic studies, suspension-adapted HEK-293 cells were grown to a density of 4×10^6 cells/mL in CD OptiCHO AGT Medium (Gibco, cat# A1122204) supplemented with 6 mM GlutaMAX (Gibco, cat# 35050061). For transient transfection, HEK-293 cells were pelleted and resuspended in FreeStyle F17 Expression Medium (Gibco, cat #A1383501) supplemented with 6 mM GlutaMAX. DNA plasmids encoding the full-length heavy and light Fab chains were incubated with PEIpro (PolyPlus, Cat# 115–100) in FreeStyle F17 Expression Medium with 6 mM GlutaMAX for 10–15 minutes at room temperature before addition to the HEK-293 cell suspension (final cell density of 4×10^6 cells/mL). Transfected cultures were maintained at 37°C in an orbital incubator shaker with humidified atmosphere containing 8% CO_2. After 24 h, transfected cultures were fed with mammalian production feed medium (2% v/v) supplemented with valproic acid (3 mM). Cultures were fed with the feed medium again on Day 2 and Day 4 (2% v/v each feed). On Day 6, supernatant was harvested and purified using a ProA affinity column, followed by a CH1-resin purification step.

Flow cytometry-based cell binding assays

To test antibody binding to CD3 on the surface of human T cells, human CD3-positive Jurkat cells (ATCC) were incubated with 100 nM IgG for 30 min on ice. After two washes with PBSF (PBS+0.1% bovine serum albumin (BSA)), IgGs were detected with goat anti-Human IgG R-PE secondary reagent (Southern Biotech, #2040–09), and analyzed by flow cytometry using a BD FACSCanto II (BD Bioscience). The FCS Express software (De Novo Software, version 5) was used for data analysis, and binding was expressed as median fluorescent intensity. This method was repeated using CD3-positive HSC-F cells to test for cyno CD3 cross-reactivity, as well as using human TCRα-knockout Jurkat cells, which keep full TCR/CD3 complexes from reaching the cell surface.[63] A secondary reagent-only staining control and human antibody IgG1 isotype-negative control were included in all experiments.

Antigen generation

Human CD3 epsilon-delta (εδ) heterodimer was produced through transient transfection in HEK293 cell lines. Plasmids were generated by insertion of the extracellular domains of human CD3 epsilon (accession #P07766, aa1–126) and human CD3 delta (accession #P04234, aa1–100) into mammalian expression vectors containing human IgG1 Fc domain with a C-terminal HIS-tag. Plasmids were transiently co-transfected into HEK293 suspension cells at a 2:1 ratio using PEIpro (Polyplus #115–100) in FreeStyle 17 medium (Gibco, #A13835–02) supplemented with 6 mM GlutaMAX (Thermo Fisher Scientific, #35050–061). Transfected cells were grown in 37°C, 8% CO2 incubator, shaking at 110 rpm. Mammalian production feed medium (2% v/v) supplemented with valproic acid (3 mM) was given to cells at 24 h, and after 3–4 d, mammalian production feed medium was given to cells again (4% v/v). After 6 d of growth, supernatant was harvested and purified in a multi-step purification scheme. First, samples were purified by a Nickel Sepharose column followed by a Sephadex G-25 (Sigma-Aldrich, #G2580) and buffer exchange into HBS pH 7.2. Samples underwent a secondary purification with a preparative Mono Q anion exchange column (Cytiva Life Sciences, #17516701), and were polished by Superdex200 size exclusion chromatography (SEC) column (Cytiva Life Sciences, #28989335). Human CD3εδ heterodimer binding to pasotuxizumab and OKT3 IgG1 was confirmed by BLI using the Octet HTX system.

Cyno CD3εδ heterodimer was produced through transient transfection in HEK293 cells. The extracellular domain sequences of cyno CD3ε (accession #Q95LI5, aa1–117) and cyno CD3 delta (CD3δ—accession #Q95LI8, aa1–100) were used to generate this antigen, as described above.

CD3ε N-terminal (N13) peptide (H2N-QDGNEEMGGITQT-OH) and its biotinylated form (H2N-QDGNEEMGGITQT(K/SCBiot(dPEG4))-amide) was sourced from BioSynth. N-terminal glutamine autocyclized to pyroglutamate (>99%), as confirmed by mass spectrometry (not shown).

CD3εδ heterodimer:antibody kinetic binding analysis by BLI

The Octet HTX system (Sartorius) was used to measure the apparent IgG binding affinities to both human and cyno CD3εδ heterodimers, as previously described.[64] All reagents were formulated in PBSF [PBS with 0.1% (w/v) BSA], and all binding steps were performed with an orbital shaking speed of 1000 rpm at 25°C. To measure IgG binding to the recombinant antigens, the antibody in a 100 nM solution was captured to an AHC (anti-human capture) sensor (Sartorius, #18–5064) to give a sensor loading of ~0.6–1.2 nm. After a short (60 s) baseline step in PBSF, the association of the antigen (100 nM) was monitored for 180 seconds. The sensors were then re-immersed in buffer for 180 seconds to monitor the dissociation of the antigen. Response values after completion of the association phase were determined using the Sartorius Analysis Software version 12.0. For response values above 0.1 nm, kinetic association and dissociation rate constants (k_{on} and k_{off}), were determined for each curve by fitting to a 1:1 binding model. The dissociation constants (K_D values) were calculated as k_{off}/k_{on}.

To measure Fab-binding affinity, recombinant Fc-antigens were loaded to AHC sensors to give a sensor loading of ~0.6–1.2 nm. After a 60 s baseline dip in buffer, the association and dissociation of Fab (100 nM) in PBSF solution was measured as detailed above. Kinetic rate constants, and subsequently the dissociation constant, were determined for Fabs eliciting response values above 0.05 nm.

CD3εδ heterodimer:antibody kinetic binding analysis by surface plasmon resonance

SPR kinetic analysis was conducted at 25°C in an HBS-EP+ running buffer system (10 mM HEPES pH 7.4, 150 mM NaCl, 3 mM EDTA, 0.05% Surfactant P20) using a Biacore 8K optical biosensor (Global Life Sciences Solutions USA, Marlborough, MA). The sample compartment was maintained at 10°C for the duration of each experiment.

For antigen on sensor, Fab in solution experiments, a goat anti-human Fc antibody (Fc-gamma specific from Jackson ImmunoResearch catalog number 109-005-098) was covalently coupled to flow cells 1 and 2 of a CM5 sensor chip surface *via* standard amine coupling (1:1 EDC:NHS) and then blocked with ethanolamine (1.0 M, pH 8.5). The CD3εδ-Fc protein (5.0 nM in running buffer) was injected (20 s at 5.0 μL/min) over flow cell 2. Six concentrations of Fab ranging from 180.0 to 0.74 nM (3-fold dilutions in running buffer) were injected (180 s at 30 μL/min) over flow cells 1 and 2. Dissociation of Fab was monitored for 600 s. Several blank buffer samples were injected (180 s at 30 μL/min) over flow cells 1 and 2 and used for reference surface subtraction. All surfaces (flow cells 1 and 2) were regenerated *via* two injections (10 s at 50 μL/min) of 10 mM glycine, pH 1.5.

For data processing and fitting, the sensorgrams were cropped to include only the association and dissociation steps. This cropped data was subsequently aligned, double reference subtracted, and then non-linear least squares fit to a 1:1 binding model using Biacore Insight Evaluation software version 3.0.11.15423.[65]

Affinity-capture self-interaction nanoparticle spectroscopy

The AC-SINS assay was performed as described previously.[20,66] In brief, gold nanoparticles (15705; Ted Pella Inc.) were coated with anti-human goat IgG Fc (109-005-098; Jackson ImmunoResearch). IgGs were then incubated with particles for 1 h and the wavelength shift was measured using Molecular Devices SpectraMax M2 with SoftMax Pro6 software. Self-interacting clones show a higher wavelength shift away from the PBS sample, indicating elevated levels of particle aggregates.

Polyreactivity assay

PSR binding of antibodies was performed as described previously.[16,19,67] Briefly, soluble membrane protein (SMP) and soluble cytosolic protein (SCP) fractions were extracted from CHO cells and biotinylated using NHS-LC-Biotin (Thermo Fisher Scientific #A39257) reagent. Yeast-presented IgGs were incubated with 1:10 diluted stock of biotinylated SMP and SCP for 20 minutes on ice, followed by two washes with PBSF, and stained with 50 μL of a secondary labeling mix containing ExtrAvidin-R-PE (Sigma-Aldrich #E4011), anti-human LC-FITC (Southern Biotech #2062–02), and propidium iodide (Sigma-Aldrich #11348639001) for 15 minutes on ice. Cells were then washed with PBSF and resuspended in PBSF for flow cytometric analysis on a BD FACS Canto II (BD Biosciences). Binding mean fluorescence intensity (MFI) was assessed with a flow cytometry analyzer and normalized to a score from 0 to 1 using three control antibodies that define low, medium, and high binding to the PSR reagent.

Calculation of theoretical pI

pI was calculated using an iterative search for the pH at which the net charge of the protein is predicted to be zero within a precision of 0.001.[68] The pKa values for the ionizable groups were obtained from EMBOSS.[69] The pI of the Fv (and IgG for IgG-like bispecific molecules) was estimated by ignoring the contributions of the C-terminal carboxylate groups in the heavy and light chains. N-terminal glutamine was assumed to be entirely converted into pyroglutamate, resulting in the loss of the free amine. Cysteine side chains participating in disulfide bonds were considered as non-ionizable.

Crystallization and X-ray data collection

Crystals of the ADI-26906 Fab complexed to CD3 epsilon N13 peptide were obtained by the sitting drop vapor diffusion method. The ADI-26906 Fab buffered in PBS, was first buffer-exchanged into 20 mM Bis-Tris pH 6.0 and 150 mM NaCl. The Fab (0.31 mM) was mixed with the N13 peptide (7.8 mM) at a Fab:peptide ratio of~1:25 and incubated on ice for 1.5 h. A BCS screen (Molecular Dimensions Ltd.) was set up using a mosquito crystallization robot (STP Labtech), with each drop consisting of 100 nL protein and 100 nL of reservoir solution, and left to equilibrate against a 40 μL reservoir solution at 20°C. After a few days, crystals were obtained in condition A6 (0.1 M MES pH 6.5, 25% w/v PEG Smear Broad).

Crystals were soaked in reservoir solution supplemented with 20% glycerol as a cryo-protectant, and flash-frozen in liquid nitrogen. X-ray diffraction data were collected at synchrotron beamline BioMAX, MAX IV Laboratory, Lund, Sweden, at 100 K and λ = 0.9763 Å. A total of 3600 images were collected with an oscillation range of 0.1° per image. The beamline is equipped with an Dectris Eiger1 16 M hybrid-pixel detector.

Structure determination, model building, and refinement

Diffraction data were indexed, integrated, scaled, and merged at the beamline using autoPROC, which includes the software XDS and Aimless.[70–72] A molecular replacement solution for the ADI-26906 Fab complexed to N13 peptide at pH 6.5 was obtained by PHASER using the heavy and light chains from natalizumab Fab (PDB: 4IRZ) where the Fv and constant regions were separated to account for changes in Fab elbow angle.[42,43] The structures were built manually in COOT and refined using PHENIX.[39–41] Data collection and refinement statistics are presented in Table S3.

Differential scanning fluorimetry to determine Tm.

Tm was determined using a CFX96 Real-Time PCR System from BioRad, based on a previously described protocol.[73] Briefly, 20 μL of 1 mg/mL sample was mixed with 10 μL of 20× SYPRO orange. The plate was scanned from 40°C to

95°C at a rate of 0.5°C/2 min. The Fab Tm was assigned using the first derivative of the raw data from the BioRad analysis software.

In vitro engineering of ADI-26906

Acidic amino acid substitutions (Asp or Glu; D/E) were introduced in the heavy and light chain CDRs of ADI-26906 using an oligo-based method. These D/E substitution oligos, which spanned all six CDRs of ADI-26906, were synthesized by IDT, covering the parent CDRs and used in various combinations, as outlined in Figure S2. Using overlap extension PCR, full-length variable heavy (VH), or light (VL) gene segments were stitched together with oligos covering heavy and light-chain framework regions 1–4. The assembled VH and VL amplicons were recombined *in situ* in *S. cerevisiae* by homologous recombination with linearized acceptor vectors to create yeast libraries of ~ 1×10^7 diversity by electroporation as previously described.[74] In total, 14 acidic amino acid substituted ADI-26906 yeast libraries were created: six with single substitutions, six with double substitutions (across two intrachain CDRs), and two with triple substitutions (across all intrachain CDRs). These 14 yeast libraries were pooled down at equal OD600 ratios into three libraries based on mutational load (Figure S2).

These single (#1), double (#2), and triple (#3) acidic amino acid substitution libraries each underwent three rounds of selection by flow cytometry. In the first round, induced yeast libraries covering at least 10-fold of their respective diversities were incubated with 100 nM of biotinylated human CD3εδ heterodimer protein under equilibrium conditions. Yeast were washed twice in PBSF (1× PBS, 0.1% [w/v] BSA), then stained with anti-human LC-FITC (Southern Biotech, #2062–02), ExtrAvidin-R-PE (Sigma-Aldrich #E4011), and propidium iodide (Invitrogen, Cat#P1304MP) for 15 minutes on ice. Labeled cells were washed twice and re-suspended in PBSF before sorting on a BD FACS Aria II (Becton Dickerson). Gates were drawn for cells with equivalent CD3εδ binding to parental clone (Figure S3). The second round was performed using biotinylated PSR as a negative selection reagent. Induced yeast libraries were incubated with a 1:10 diluted stock of PSR for 20 minutes on ice, followed by the same wash and secondary detection steps as described above. Gates were drawn for cells without binding to the PSR reagent (Figure S3). In the terminal round, induced yeast libraries were incubated with 100, 10, or 1 nM of biotinylated CD3ε N13 peptide under equilibrium conditions. Gates were drawn for cells with equivalent or improved CD3 binding compared to the parental clone and sorted yeast were plated for single colony isolation and sequencing (Figure S3).

Generation of bispecific constructs

IgG-like (1 + 1) bispecific antibodies were produced in CHO-K1 cells after transient transfection with four expression vectors encoding a CD20 or HEL antigen-binding heavy chain, a CD20 or HEL antigen-binding light chain, a CD3-binding heavy chain, and a CD3-binding light chain. HC/LC pairing and CH3 heterodimerization mutations were introduced to facilitate recovery of heterodimers (details disclosed in the patent literature).[75,76] Bispecific antibody molecules were harvested from culture supernatants and purified by ProA affinity chromatography followed by Mono S cation exchange polishing using a linear pH gradient as previously described.[77] Purified bispecifics were characterized by liquid chromatography-mass spectrometry (LC/MS), analytical SEC, and analytical IEX. Bispecific molecules purified by ProA and subsequent cation exchange as described above, were shown to contain less than 1% homodimer and less than 1% aggregates. Endotoxin levels were measured using a limulus amebocyte lysate assay (Charles River Laboratories) and were shown to be below 0.1 EU/mg.

Jurkat stimulation assay and IL-2 secretion with monospecific IgGs

IgG dilutions were aliquoted (200 µl) into Nunc-Immuno™ Maxisorp 96-well plates (Thermo Fisher) and stored at 4°C overnight. Plates were centrifuged (500 g for 5 min at 4°C) and washed 3 times with 200 µl of ice-cold sterile Dulbecco's PBS (DPBS). Human Jurkat cells (Clone E6–1, ATCC) were thawed and washed 3 times in 50 ml warm (37°C) cell culture medium (Gibco RPMI Medium 1640 GlutaMAX-I) and FBS (Avantor ® Seradigm #89510–186, lot 184B19) at pH 7.4. Cells (200 µl) were aliquoted into IgG-bound plates (20,000 cells/well) and incubated overnight at 37°C with 5% CO2. An anti-CD28 antibody (Ultra-LEAF™, CD28.2, BioLegend) was included in the culture media at a concentration of 2 µg/µl prior to plating for CD28+ conditions. The contents of each well were subsequently resuspended, transferred to a 96-well V-bottom plate (Greiner Bio-One), and centrifuged (500 g for 5 min at 4°C), followed by harvest and freezing of the supernatant at −20°C.

IL-2 was quantified by a V-PLEX Human IL-2 Kit (Meso Scale Discovery) according to the manufacturer's instructions. Briefly, 2-fold dilutions of the supernatant in Diluent 2 were prepared in a 96-well V-bottom plate (Greiner Bio-One). 50 µl of the diluted supernatants were transferred to an MSD plate (Meso Scale Discovery) and incubated on a plate shaker at 700 rpm at room temperature (22–25°C) for 2 h. Plates were washed 3 times, followed by addition of 25 µl IL-2 detection antibody and incubation for 1–2 h at 700 rpm at room temperature (22–25°C). Antibody solution was discarded and 150 µl of read buffer with surfactant was added to each well. IL-2 levels in each well were subsequently measured on a Meso Sector S 600 MM instrument (Meso Scale Discovery).

To detect CD25 and CD69 expression, pelleted cells were resuspended in 50 µl staining solution containing 1:100 CD2-FITC, 1:100 CD25-PE, 1:100 CD69-APC, 1:500 PI diluted in PBSF and incubated for 20 minutes on ice. All staining antibodies were sourced from BioLegend: CD2 (clone SK3), CD25 (clone BC69), and CD69 (clone FN50). Stained cells were washed 2.5× in 200 µl PBSF (500 g for 5 min at 4°C) and resuspended in 60 µl PBSF before analyzing 30 µl per sample on a BD FACSCelesta™ Cell Analyzer (BD Biosciences).

Jurkat (NFAT-luc) T cell activation bioassay

Jurkat T cells genetically engineered to express a luciferase reporter driven by a nuclear factor of activated T cells (NFAT) response element were purchased from Promega

(#J1625). In this bioassay, activation of NFAT can be mediated by bispecific antibody simultaneously binding CD3 on the reporter T cells and a TAA expressed on a tumor cell. Serial dilutions of CD20 × CD3, HEL × CD3, and CD20 × HEL bispecific antibodies were added to Jurkat (NFAT-luc) cells (100,000 cells/well) in the presence of CD20-expressing Raji cells (20,000 cells/well) following manufacturer's instructions. All bispecific antibody dilutions and the bioassay were performed in assay buffer consisting of RPMI 1640 medium supplemented with 10% FBS. Plates were incubated at 37°C in a humidified 5% CO2 incubator for 6 h before being brought to room temperature for 15 minutes. Bio-Glo™ Reagent (Promega) was then added to each well and incubated at room temperature for 10 minutes after which luminescence was measured using an EnSpire multimode plate reader (PerkinElmer). Data were analyzed by a variable slope four parameter equation using GraphPad Prism version 9.3.1 for Windows.

Ex-vivo T cell expansion

Frozen, naïve primary human CD8 + CD45RA + cells were purchased from StemCell Technologies (catalog number 70,030, lot 200173103C). T cells were thawed and seeded at 1×10^6 cells/mL in 24-well plates containing ImmunoCult™-XF T Cell Expansion Medium (StemCell Technologies catalog number 10,981) supplemented with 10 ng/mL recombinant human IL-2 (StemCell Technologies catalog number 78,036). ImmunoCult™ Human CD3/CD28/CD2 T Cell Activator (StemCell Technologies catalog number 10,990) was added at 25 ml per mL of expansion medium on day 0 after which plates were placed in a 37°C 5% CO2 incubator. On days 3, 5 and 7 fresh medium containing 10 ng/mL IL-2 was added to maintain cell densities between 1.5 and 4×10^5 cells/mL following the manufacturer's recommendations. At day 10, expanded cells were harvested and cryopreserved in Cryostor5 medium (StemCell Technologies catalog number 7933).

In-vitro flow cytometry RTCC assay

CD20-expressing Raji cells were labeled with 0.5 mM CellTracker™ Violet BMQC fluorescent tracking dye (Invitrogen). Labeled Raji cells (10,000 cells/well) were plated in flat-bottom 96-well plates (Costar, #3596) along with pre-activated, expanded human CD8+ T cells at effector:target ratios of 10:1 and 2:1 in complete media (RPMI, 10% FBS, 2% GlutaMax). Serial dilutions of CD20 × CD3, HEL × CD3, and CD20 × HEL bispecific antibodies prepared in complete media were added and plates were allowed to incubate for 24–48 h at 37°C, 5% CO2. At the end of the incubation period, cells were lifted to V-bottom plates and centrifuged for 5 minutes at 500 g. Culture supernatants were harvested for multiplexed cytokine analysis by MSD following vendor instructions. The remaining cells were washed with cold PBSF and stained with an antibody cocktail containing CD2-FITC, CD25-PE, CD69-APC, and propidium iodide (PI) for 30 minutes at 4°C. Cells were washed twice, resuspended in cold PBSF and analyzed by flow cytometry on a BD FACSCelesta™ Cell Analyzer (BD Biosciences). Gating on PI

negative, CellTracker Violet positive cells allowed quantification of surviving Raji cells. The percent live population was used to calculate % cytotoxicity as: ([% of live Raji cells without treatment – % of live Raji cells with treatment]/[% Raji cells without treatment]) × 100%. Simultaneously, CD8+ T cell activation was assessed by gating on viable CellTracker Violet negative cells that expressed CD2. Activation is expressed as the percentage of CD2+ cells co-expressing CD25 and CD69.

Abbreviations

AC-SINS	affinity-capture self-interaction nanoparticle spectroscopy
Fv	antibody variable fragment
VH	antibody variable heavy
VL	antibody variable light
Fab	antigen binding fragment
k_{on}	association rate
ASU	asymmetric unit
BVP	Baculovirus Particle
BLI	biolayer interferometry
CD3ε	CD3 epsilon
N13	CD3ε N-terminal peptide
CHO	Chinese hamster ovary
CDRs	complementarity-determining regions
Fc	constant fragment
HSC-F	Cyno macaque suspension T-cells
cyno	cynomolgus monkey
CRS	cytokine release syndrome
DSF	differential scanning fluorimetry
K_D	dissociation constant
k_{off}	dissociation rate
DPBS	Dulbecco's phosphate-buffered saline
εδ	epsilon-delta
HEL	hen egg lysozyme
IgG1	immunoglobulin G1
INNs	International Nonproprietary Names
IEX	ion exchange chromatography
pI	isoelectric point
LC/MS	liquid chromatography mass spectrometry
MFI	mean fluorescence intensity
mAbs	monoclonal antibodies
NHP	non-human primate
NFAT	nuclear factor of activated T cells
PK	pharmacokinetic
PSR	poly-specificity reagent
P.F.	poor fit
ProA	Protein A
RTCC	redirected T cell cytotoxicity
RMSD	root-mean-squared deviation
SEC	size exclusion chromatography
SCP	soluble cytosolic protein
SMP	soluble membrane protein
SASA	solvent-accessible surface area
SPR	surface plasmon resonance
TCR	T-cell receptor
TAA	tumor-associated antigen
WHO	World Health Organization

Author contributions

Conceptualization, R.P., P.F.W., and M.B.B.; Methodology, M.B.B.; Validation, C.Y.L., M.W., and M.B.B.; Formal Analysis, C.Y.L. and M.B.B.; Investigation, C.Y.L., C.L.A., M.E.B., L.Z., and M.B.B.; Writing – Original Draft Preparation, C.Y.L. and M.B.B.; Writing – Review & Editing, E.K., R.P., P.F.W., and M.B.B.; Visualization, C.Y.L. and M.B.B.; Supervision, R.P., P.F.W., and M.B.B.; Project Administration, R.P., P.F.W., and M.B.B.

Disclosure statement

C.Y.L., C.L.A., M.E.B., L.Z., E.M.K., R.P., P.F.W., and M.B.B. are employees of Adimab, LLC and may hold shares in Adimab, LLC. E.M.K., R.P., and M.B.B. are authors on patents and patent applications describing the engineered CD3 antibodies.

Funding

ORCID

Michael B Battles ⓘD http://orcid.org/0000-0002-5321-7460

Data availability statement

Coordinates and structure factors for ADI-26906-Fab complexed to the CD3ε-N13 peptide @ pH 6.5 have been deposited in the Protein Data Bank under accession code 8F0L. https://doi.org/10.2210/pdb8F0L/pdb. All other data are available in the manuscript or supplementary materials.

References

1. Zhou S, Liu M, Ren F, Meng X, Yu J. The landscape of bispecific T cell engager in cancer treatment. Biomarker Res. 2021;9:38. doi:10.1186/s40364-021-00294-9. pmid = 34039409, pmcid = PMC8157659.

2. Baeuerle PA, Reinhardt C. Bispecific T-Cell engaging antibodies for cancer therapy. Cancer Res. 2009;69:4941–44. doi:10.1158/0008-5472.can-09-0547. pmid = 19509221.

3. Demaria O, Gauthier L, Debroas G, Vivier E. Natural killer cell engagers in cancer immunotherapy: next generation of immuno-oncology treatments. Eur J Immunol. 2021;51:1934–42mid = 34145579. doi:10.1002/eji.202048953.

4. Tian Z, Liu M, Zhang Y, Wang X. Bispecific T cell engagers: an emerging therapy for management of hematologic malignancies. J Hematol Oncol. 2021;14:75. doi:10.1186/s13045-021-01084-4. pmid = 33941237, pmcid = PMC8091790.

5. Bargou R, Leo E, Zugmaier G, Klinger M, Goebeler M, Knop S, Noppeney R, Viardot A, Hess G, Schuler M, et al. Tumor regression in cancer patients by very low doses of a T cell–Engaging antibody. Science. 2008;321:974–77mid = 18703743. doi:10.1126/science.1158545.

6. Kaplon H, Crescioli S, Chenoweth A, Reichert JV, Janice M. Antibodies to watch in 2023. mAbs. 2023. doi:10.1080/19420862.2022.2153410.

7. Ledbetter JA, Gentry LE, June CH, Rabinovitch PS, Purchio AF. Stimulation of T cells through the CD3/T-cell receptor complex: role of cytoplasmic calcium, protein kinase C translocation, and phosphorylation of pp60c-src in the activation pathway. Mol Cell Biol. 1987;7:650–56. doi:10.1128/mcb.7.2.650-656.1987. pmid = 2434833, pmcid = PMC365120.

8. Cibrián D, Sánchez-madrid F. CD69: from activation marker to metabolic gatekeeper. Eur J Immunol. 2017;47:946–53. doi:10.1002/eji.201646837. pmid = 28475283, pmcid = PMC6485631.

9. González-Amaro R, Cortés JR, Sánchez-Madrid F, Martín P. Is CD69 an effective brake to control inflammatory diseases? Trends Mol Med. 2013;19:625–32. doi:10.1016/j.molmed.2013.07.006. pmid = 23954168, pmcid = PMC4171681.

10. Li J, Stagg NJ, Johnston J, Harris MJ, Menzies SA, DiCara D, Clark V, Hristopoulos M, Cook R, Slaga D, et al. Membrane-Proximal epitope facilitates efficient T cell synapse formation by anti-FcRH5/CD3 and is a requirement for myeloma cell killing. Cancer Cell. 2017;31:383–95. pmid = 28262555, pmcid = PMC5357723. doi:10.1016/j.ccell.2017.02.001.

11. Razvag Y, Neve-Oz Y, Sajman J, Reches M, Sherman E. Nanoscale kinetic segregation of TCR and CD45 in engaged microvilli facilitates early T cell activation. Nat Commun. 2018;9:732. doi:10.1038/s41467-018-03127-w. pmid = 29467364, pmcid = PMC5821895.

12. Clynes RA, Desjarlais JR. Redirected T cell cytotoxicity in cancer therapy. Annu Rev Med. 2018;70:1–14mid = 30379598. doi:10.1146/annurev-med-062617-035821.

13. Hötzel I, Theil F-P, Bernstein LJ, Prabhu S, Deng R, Quintana L, Lutman J, Sibia R, Chan P, Bumbaca D, et al. A strategy for risk mitigation of antibodies with fast clearance. mAbs. 2012;4:753–60. pmid = 23778268, pmcid = PMC3502242. doi:10.4161/mabs.22189.

14. Jain T, Sun T, Durand S, Hall A, Houston NR, Nett JH, Sharkey B, Bobrowicz B, Caffry I, Yu Y, et al. Biophysical properties of the clinical-stage antibody landscape. Proceedings of the National Academy of Sciences. 2017; 114:944–49. doi:10.1073/pnas.1616408114, pmid = 28096333.

15. Tessier PM, Jinkoji J, Cheng Y-C, Prentice JL, Lenhoff AM. Self-Interaction nanoparticle spectroscopy: a nanoparticle-based protein interaction assay. J Am Chem Soc. 2008;130:3106–12. doi:10.1021/ja077624q. pmid = 18271584.

16. Shehata L, Maurer DP, Wec AZ, Lilov A, Champney E, Sun T, Archambault K, Burnina I, Lynaugh H, Zhi X, et al. Affinity maturation enhances antibody specificity but compromises conformational stability. Cell Rep. 2019;28:3300–8.e3304mid = 31553901. doi:10.1016/j.celrep.2019.08.056.

17. Avery LB, Wade J, Wang M, Tam A, King A, Piche-Nicholas N, Kavosi MS, Penn S, Cirelli D, Kurz JC, et al. Establishing in vitro in vivo correlations to screen monoclonal antibodies for physico-chemical properties related to favorable human pharmacokinetics. mAbs. 2017;10: pmid = 29271699, pmcid = PMC5825195. doi:10.1080/19420862.2017.1417718.

18. Kraft TE, Richter WF, Emrich T, Knaupp A, Schuster M, Wolfert A, Kettenberger H. Heparin chromatography as an in vitro predictor for antibody clearance rate through pinocytosis. mAbs. 2019;12:1683432. doi:10.1080/19420862.2019.1683432. pmid = 31769731, pmcid = PMC6927760.

19. Xu Y, Roach W, Sun T, Jain T, Prinz B, T-Y Y, Torrey J, Thomas J, Bobrowicz P, Vásquez M, et al. Addressing polyspecificity of antibodies selected from an in vitro yeast presentation system: a FACS-based, high-throughput selection and analytical tool. Protein Eng Design Select. 2013;26:663–70. pmid = 24046438. doi:10.1093/protein/gzt047.

20. Liu Y, Caffry I, Wu J, Geng SB, Jain T, Sun T, Reid F, Cao Y, Estep P, Yu Y, et al. High-throughput screening for developability during early-stage antibody discovery using self-interaction nanoparticle spectroscopy. mAbs. 2013;6:483–92. pmid = 24492294, pmcid = PMC3984336. doi:10.4161/mabs.27431.

21. Ausserwöger H, Schneider MM, Herling TW, Arosio P, Invernizzi G, Knowles TPJ, Lorenzen N. Non-specificity as the sticky problem in therapeutic antibody development. Nat Rev Chem. 2022;1–18. doi:10.1038/s41570-022-00438-x.

22. Cunningham O, Scott M, Zhou ZS, Finlay WJJ. Polyreactivity and polyspecificity in therapeutic antibody development: risk factors for failure in preclinical and clinical development campaigns.

mAbs. 2021;13:1999195mid = 34780320. doi:10.1080/19420862. 2021.1999195.

23. Mouquet H, Scheid JF, Zoller MJ, Krogsgaard M, Ott RG, Shukair S, Artyomov MN, Pietzsch J, Connors M, Pereyra F, et al. Polyreactivity increases the apparent affinity of anti-HIV antibodies by heteroligation. Nature. 2010;467:591–95. pmid = 20882016, pmcid = PMC3699875. doi:10.1038/nature09385.

24. Yadav R, Sukumaran S, Zabka TS, Li J, Oldendorp A, Morrow G, Reyes A, Cheu M, Li J, Wallin JJ, et al. Nonclinical pharmacokinetics and pharmacodynamics characterization of anti-CD79b/ CD3 T Cell-Dependent bispecific antibody using a surrogate molecule: a potential therapeutic agent for B cell malignancies. Pharmaceutics. 2022;14:970. pmid = 35631556, pmcid = PMC9147001. doi:10.3390/pharmaceutics14050970.

25. Haber L, Olson K, Kelly MP, Crawford A, DiLillo DJ, Tavaré R, Ullman E, Mao S, Canova L, Sineshchekova O, et al. Generation of T-cell-redirecting bispecific antibodies with differentiated profiles of cytokine release and biodistribution by CD3 affinity tuning. Sci Rep. 2021;11:14397mid = 34257348. doi:10.1038/s41598-021-93842-0.

26. Mandikian D, Takahashi N, Lo AA, Li J, Eastham-Anderson J, Slaga D, Ho J, Hristopoulos M, Clark R, Totpal K, et al. Relative target affinities of T-Cell–dependent bispecific antibodies determine biodistribution in a solid tumor mouse model. Mol Cancer Ther. 2018;17:molcanther.0657.2017. pmid = 29339550. doi:10. 1158/1535-7163.mct-17-0657.

27. Poussin M, Sereno A, Wu X, Huang F, Manro J, Cao S, Carpenito C, Glasebrook A Jr, Demarest S, Demarest SJ. Dichotomous impact of affinity on the function of T cell engaging bispecific antibodies. J ImmunoTher Cancer. 2021;9:e002444. pmid = 34253637, pmcid = PMC8276301. doi:10.1136/jitc-2021-002444.

28. Staflin K, Zafra CLZD, Schutt LK, Clark V, Zhong F, Hristopoulos M, Clark R, Li J, Mathieu M, Chen X, et al. Target arm affinities determine preclinical efficacy and safety of anti-HER2/CD3 bispecific antibody. JCI Insight. 2020;5:e133757. pmid = 32271166, pmcid = PMC7205277. doi:10.1172/jci.insight. 133757.

29. Bortoletto N, Scotet E, Myamoto Y, D'oro U, Lanzavecchia A. Optimizing anti-cd3 affinity for effective T cell targeting against tumor cells. Eur J Immunol. 2002;32:3102–07. doi:10.1002/1521-4141(200211)32:11<3102:aid-immu3102>3.0.co;2-c. pmid = 12385030.

30. Ellerman D. Bispecific T-cell engagers: towards understanding variables influencing the in vitro potency and tumor selectivity and their modulation to enhance their efficacy and safety. Methods. 2019;154:102–17. pmid = 30395966. doi:10.1016/j. ymeth.2018.10.026.

31. Zorn JA, Wheeler ML, Barnes RM, Kaberna J, Morishige W, Harris M, Huang RYC, Lohre J, Chang YC, Chau B, et al. Humanization of a strategic CD3 epitope enables evaluation of clinical T-cell engagers in a fully immunocompetent in vivo model. Sci Rep. 2022;12:3530mid = 35241687. doi:10.1038/s41598-022-06953-7.

32. Camacho CJ, Kimura SR, DeLisi C, Vajda S. Kinetics of Desolvation-Mediated Protein–Protein Binding. Biophys J. 2000;78:1094–105. doi:10.1016/s0006-3495(00)76668-9. pmid = 10692300, pmcid = PMC1300713.

33. Bogan AA, Thorn KS. Anatomy of hot spots in protein interfaces11edited by J. Wells. J Mol Biol. 1998;280:1–9. doi:10.1006/jmbi. 1998.1843. pmid = 9653027.

34. The antibody society. Therapeutic monoclonal antibodies approved or in regulatory review. [accessed June 15, 2020].

35. Chen Xiaocheng, Dennis Mark S, Ebens, Jr Allen J, Junttila, Teemu T, Kelley Robert F, Mathieu Mary A, Sun Liping L. 2015. Anti-CD3 antibodies and methods of use. US10174124B2.

36. Datta-Mannan A, Lu J, Witcher DR, Leung D, Tang Y, Wroblewski VJ. The interplay of non-specific binding, target-mediated clearance and FcRn interactions on the pharmacokinetics of humanized antibodies. mAbs. 2015;7:1084–93.

doi:10.1080/19420862.2015.1075109. pmid = 26337808, pmcid = PMC4966429.

37. Igawa T, Tsunoda H, Tachibana T, Maeda A, Mimoto F, Moriyama C, Nanami M, Sekimori Y, Nabuchi Y, Aso Y, et al. Reduced elimination of IgG antibodies by engineering the variable region. Protein Eng Design Select. 2010;23:385–92mid = 20159773. doi:10.1093/protein/gzq009.

38. Li B, Tesar D, Boswell CA, Cahaya HS, Wong A, Zhang J, Meng YG, Eigenbrot C, Pantua H, Diao J, et al. Framework selection can influence pharmacokinetics of a humanized therapeutic antibody through differences in molecule charge. mAbs. 2014;6:1255–64. pmid = 25517310, pmcid = PMC4623330. doi:10.4161/mabs.29809.

39. Adams PD, Afonine PV, Bunkóczi G, Chen VB, Davis IW, Echols N, Headd JJ, Hung LW, Kapral GJ, Grosse-Kunstleve RW, et al.Zwart\it PHENIX: a comprehensive Python-based system for macromolecular structure solution. Acta Crystallographica Section D. 2010; 66:213–21. doi:10.1107/S0907444909052925.

40. Emsley Bl P, Scott WG, Cowtan K, Cowtan K. Features and development of Coot. Acta Crystal Sec D. 2010;66:486–501. doi:10.1107/S0907444910007493.

41. Emsley P, Cowtan K. Cowtan PEaK.\it Coot: model-building tools for molecular graphics. Acta Crystal Sec D. 2004;60:2126–32. doi:10.1107/S0907444904019158.

42. McCoy RWG-K AJ, Adams PD, Winn MD, Storoni LC, Storoni LC, Read RJ. Phaser crystallographic software. J App Crystal. 2007;40:658–74. doi:10.1107/S0021889807021206.

43. Yu Y, Schürpf T, Springer TA. How Natalizumab Binds and Antagonizes α4 Integrins*. J Biol Chem. 2013;288:32314–25. doi:10.1074/jbc.m113.501668. pmid = 24047894.

44. Sheffler W, Baker D. RosettaHoles: rapid assessment of protein core packing for structure prediction, refinement, design, and validation. Protein Sci. 2009;18:229–39. doi:10.1002/pro.8. pmid = 19177366, pmcid = PMC2708028.

45. Kjer-Nielsen L, Dunstone MA, Kostenko L, Ely LK, Beddoe T, Mifsud NA, Purcell AW, Brooks AG, McCluskey J, Rossjohn J Crystal structure of the human T cell receptor CD3εγ heterodimer complexed to the therapeutic mAb OKT3. Proceedings of the National Academy of Sciences. 2004; 101:7675–80. doi:10.1073/ pnas.0402295101, pmid = 15136729, pmcid = PMC419665.

46. Arnett KL, Harrison SC, Wiley DC Crystal structure of a human CD3-ε/δ dimer in complex with a UCHT1 single-chain antibody fragment. Proceedings of the National Academy of Sciences of the United States of America. 2004; 101:16268–73. doi:10.1073/pnas. 0407359101, pmid = 15534202.

47. Dong D, Zheng L, Lin J, Zhang B, Zhu Y, Li N, Xie S, Wang Y, Gao N, Huang Z. Structural basis of assembly of the human T cell receptor–cd3 complex. Nature. 2019;573:546–52mid = 31461748. doi:10.1038/s41586-019-1537-0.

48. Sušac L, Vuong MT, Thomas C, Bülow Sv OB, Santos C, Am FR, Hummer G, Tampé R, Davis SJ, Davis SJ. Structure of a fully assembled tumor-specific T cell receptor ligated by pMHC. Cell. 2022;185:3201–13.e3219. doi:10.1016/j.cell.2022.07.010.

49. Chen Y, Zhu Y, Li X, Gao W, Zhen Z, Dong D, Huang B, Ma Z, Zhang A, Song X, et al. Cholesterol inhibits TCR signaling by directly restricting TCR-CD3 core tunnel motility. Mol Cell. 2022;82:1278–87.e1275mid = 35271814. doi:10.1016/j.molcel. 2022.02.017.

50. Jurrus E, Engel D, Star K, Monson K, Brandi J, Felberg LE, Brookes DH, Wilson L, Chen J, Liles K, et al. Improvements to the APBS biomolecular solvation software suite. Protein Sci. 2018;27:112–28. pmid = 28836357, pmcid = PMC5734301, eprint = 1707.00027. doi:10.1002/pro.3280.

51. Liu YD, Goetze AM, Bass RB, Flynn GC. N-terminal Glutamate to Pyroglutamate Conversion in vivo for Human IgG2 Antibodies. J Biol Chem. 2011;286:11211–17. doi:10.1074/jbc.m110.185041. pmid = 21282104, pmcid = PMC3064176.

52. Leong SR, Sukumaran S, Hristopoulos M, Totpal K, Stainton S, Lu E, Wong A, Tam L, Newman R, Vuillemenot BR, et al. An anti-CD3/anti–CLL-1 bispecific antibody for the treatment of acute

myeloid leukemia. Blood. 2017;129:609–18. doi:10.1182/blood-2016-08-735365. pmid = 27908880, pmcid = PMC5290988.

53. Yadav S, Laue TM, Kalonia DS, Singh SN, Shire SJ. The influence of charge distribution on self-Association and viscosity behavior of monoclonal antibody solutions. Mol Pharm. 2012;9:791–802mid = 22352470. doi:10.1021/mp200566k.

54. Birtalan S, Zhang Y, Fellouse FA, Shao L, Schaefer G, Sidhu SS. The intrinsic contributions of tyrosine, serine, glycine and arginine to the affinity and specificity of antibodies. J Mol Biol. 2008;377:1518–28. doi:10.1016/j.jmb.2008.01.093. pmid = 18336836.

55. DeKosky BJ, Lungu OI, Park D, Johnson EL, Charab W, Chrysostomou C, Kuroda D, Ellington AD, Ippolito GC, Gray JJ, et al. Large-scale sequence and structural comparisons of human naive and antigen-experienced antibody repertoires. Proceedings of the National Academy of Sciences. 2016; 113:E2636–45. doi:10.1073/pnas.1525510113, pmid = 27114511, pmcid = PMC4868480.

56. Sheinerman FB, Norel R, Honig B. Electrostatic aspects of protein–protein interactions. Curr Opin Struct Biol. 2000;10:153–59. doi:10.1016/s0959-440x(00)00065-8. pmid = 10753808.

57. Marvin JS, Lowman HB. Redesigning an antibody fragment for faster association with its antigen. Biochemistry. 2003;42:7077–83mid = 12795603. doi:10.1021/bi026947q.

58. Gabdoulline RR, Wade RC. Biomolecular diffusional association. Curr Opin Struct Biol. 2002;12:204–13mid = 11959498. doi:10.1016/s0959-440x(02)00311-1.

59. Bugelski PJ, Achuthanandam R, Capocasale RJ, Treacy G, Bouman-Thio E. Monoclonal antibody-induced cytokine-release syndrome. Expert Rev Clin Immunol. 2009;5:499–521. doi:10.1586/eci.09.31. pmid = 20477639.

60. Dudgeon K, Rouet R, Kokmeijer I, Schofield P, Stolp J, Langley D, Stock D, Christ D General strategy for the generation of human antibody variable domains with increased aggregation resistance. Proceedings of the National Academy of Sciences. 2012; 109:10879–84. doi:10.1073/pnas.1202866109, pmid = 22745168, pmcid = PMC3390889.

61. Perchiacca JM, Ladiwala ARA, Bhattacharya M, Tessier PM. Aggregation-resistant domain antibodies engineered with charged mutations near the edges of the complementarity-determining regions. Protein Eng Design Select. 2012;25:591–602mid = 22843678. doi:10.1093/protein/gzs042.

62. Wec AZ, Wrapp D, Herbert AS, Maurer DP, Haslwanter D, Sakharkar M, Jangra RK, Dieterle ME, Lilov A, Huang D, et al. Broad neutralization of SARS-related viruses by human monoclonal antibodies. Science. 2020;369:731–36mid = 32540900. doi:10.1126/science.abc7424.

63. Akari H, Nam K-H, Mori K, Otani I, Shibata H, Adachi A, Terao K, Yoshikawa Y. Effects of SIVmac Infection on Peripheral Blood CD4+CD8+T Lymphocytes in Cynomolgus Macaques. Clin Immun. 1999;91:321–29mid = 10370378. doi:10.1006/clim.1999.4700.

64. Sakharkar M, Rappazzo CG, Wieland-Alter WF, Hsieh C-L, Wrapp D, Esterman ES, Kaku CI, Wec AZ, Geoghegan JC, McLellan JS, et al. Prolonged evolution of the human B cell response to SARS-CoV-2 infection. Sci Immun. 2021;6:eabg6916. pmid = 33622975, pmcid = PMC8128290. doi:10.1126/sciimmunol.abg6916.

65. Myszka DG. Improving biosensor analysis. J Mol Recogn. 1999;12:279–84. doi:10.1002/(sici)1099-1352(199909/10)12:5<279:aid-jmr473>3.0.co;2-3. pmid = 10556875.

66. Sule Shantanu V, Sukumar M, Weiss William F, Marcelino-Cruz Anna M, Sample T, Tessier Peter M. High-Throughput analysis of concentration-Dependent antibody self-Association. Biophys J. 2011;101:1749–57. doi:10.1016/j.bpj.2011.08.036. pmid = 21961601, pmcid = PMC3183799.

67. Kelly RL, Geoghegan JC, Feldman J, Jain T, Kauke M, Le D, Zhao J, Wittrup KD. Chaperone proteins as single component reagents to assess antibody nonspecificity. mAbs. 2017;9:1036–40. doi:10.1080/19420862.2017.1356529. pmid = 28745541, pmcid = PMC5627595.

68. Kozlowski LP. IPC – Isoelectric point calculator. Biol Direct. 2016;11:55. doi:10.1186/s13062-016-0159-9. pmid = 27769290, pmcid = PMC5075173.

69. EMBOSS. Date.

70. Evans PR, Murshudov GN, GN EPaM. How good are my data and what is the resolution? Acta Crystal Sec D. 2013;69:1204–14. doi10.1107/S0907444913000061.

71. Kabsch W. It XDS. Acta crystallographica section D. Acta Crystallogr D Biol Crystallogr. 2010;66(2):125–32. doi:10.1107/S0907444909047337.

72. Vonrhein C, Cf PK, Sharff O, Smart A, Paciorek T, Womack W, Bricogne G, Bricogne G. Data processing and analysis with the autoPROC toolbox. Acta Crystal Sec D. 2011;67:293–302. doi:10.1107/S0907444911007773.

73. He F, Woods CE, Becker GW, Narhi LO, Razinkov VI., Razinkov VI. High-throughput assessment of thermal and colloidal stability parameters for monoclonal antibody formulations. J Pharm Sci. 2011;100:5126–41. doi:10.1002/jps.22712.

74. Rappazzo CG, Tse LV, Kaku CI, Wrapp D, Sakharkar M, Huang D, Deveau LM, Yockachonis TJ, Herbert AS, Battles MB, et al. Broad and potent activity against SARS-like viruses by an engineered human monoclonal antibody. Science. pp.eabf4830. 2021. doi:10.1126/science.abf4830

75. Stein C, Pejchal R, Mccreary J, Barlow K, Sivasubramanian A, Battles MB inventors; Adimab; WO2022150785A2s assignee. ^assignees. variant Ch3 Domains engineered for preferential Ch3 heterodimerization, multi-Specific antibodies comprising the same, and methods of making thereof.

76. Barlow K, Sivasubramanian A, Battles MB inventors; Adimab; WO2022150787A2s assignee.^assignees. Variant Ch1 Domains and Variant Cl Domains engineered for preferential chain pairing and multi-specific antibodies comprising the same.

77. Sharkey B, Pudi S, Moyer IW, Zhong L, Prinz B, Baruah H, Lynaugh H, Kumar S, Wittrup KD, Nett JH. Purification of common light chain IgG-like bispecific antibodies using highly linear pH gradients. mAbs. 2017;9:257–68. doi:10.1080/19420862.2016.1267090. pmid = 27937066, pmcid = PMC5297495.